Article

Caffeine Improves the Performance and Thermal Stability of Perovskite Solar Cells

Rui Wang, Jingjing Xue, Lei Meng, ..., Yonghai Yuan, Yu Huang, Yang Yang

zkwang@suda.edu.cn (Z.-K.W.)
yangy@ucla.edu (Y.Y.)

HIGHLIGHTS

Caffeine enhances both thermal stability and efficiency

The stabilized power conversion efficiency of 19.8% was realized

Thermally stable solar cells at 85°C for over 1,300 h were achieved

"Perovskite is drinking coffee." The perfect temperature to serve coffee is 85°C. The authors here introduced caffeine, which is the active material of coffee, into the active materials of the perovskite solar cells to enhance their performance and thermal stability under 85°C. A champion-stabilized efficiency of 19.8% with 1,300 h thermal stability at 85°C in nitrogen was achieved. This simple, cost-effective, and generalized strategy increases the commercial prospects of perovskite solar cells.

Joule

CellPress

Article

Caffeine Improves the Performance and Thermal Stability of Perovskite Solar Cells

Rui Wang,[1,5] Jingjing Xue,[1,5] Lei Meng,[1] Jin-Wook Lee,[1] Zipeng Zhao,[1] Pengyu Sun,[1] Le Cai,[1] Tianyi Huang,[1] Zhengxu Wang,[1] Zhao-Kui Wang,[1,2,*] Yu Duan,[1,3] Jonathan Lee Yang,[1,6] Shaun Tan,[1] Yonghai Yuan,[4] Yu Huang,[1] and Yang Yang[1,7,*]

SUMMARY

To increase the commercial prospects of metal halide perovskite solar cells, there is a need for simple, cost-effective, and generalized approaches that mitigate their intrinsic thermal instability. Here we show that 1,3,7-trimethylxanthine, a commodity chemical with two conjugated carboxyl groups better known by its common name caffeine, improves the performance and thermal stability of perovskite solar cells based on both $MAPbI_3$ and $CsFAMAPbI_3$ active layers. The strong interaction between caffeine and Pb^{2+} ions serves as a "molecular lock" that increases the activation energy during film crystallization, delivering a perovskite film with preferred orientation, improved electronic properties, reduced ion migration, and greatly enhanced thermal stability. Planar n-i-p solar cells based on caffeine-incorporated pure $MAPbI_3$ perovskites, which are notoriously unstable, exhibit a champion-stabilized efficiency of 19.8% and retain over 85% of their efficiency under continuous annealing at 85°C in nitrogen.

INTRODUCTION

Organic-inorganic hybrid halide perovskite (PVSK) materials have attracted considerable attention because of their unique photoelectric properties, which can be applied to an extensive variety of applications.[1–6] Particularly, PVSK materials have been applied to photovoltaics with promising results and have shown rapid development.[7–11] Within only a few years, the power conversion efficiency (PCE) of PVSK solar cells has been enhanced from 3.8% to 23.3%.[12–15] Despite the tremendous achievements that have been made toward pushing the efficiency, long-term stability is still the challenge for the commercialization of PVSK solar cells.[16–21] Specifically, the black phase of cesium (Cs)- and formamidinium (FA)-based PVSKs are thermodynamically unfavorable at room temperature[22,23] such that methylammonium (MA)-based PVSK may be the ideal candidate for the commercialization of PVSK solar cells since the tetragonal black phase of MA PVSKs are stable at low temperatures.[24] However, the intrinsically volatile nature of the MA organic cation will lead to the rapid decomposition of PVSK and precipitate trigonal PbI_2 at elevated temperatures.[25,26] In the meantime, there are numerous under-coordinated ions in the PVSK, as is common in most ionic crystals.[27] For example, I^- ions will easily migrate through the polycrystalline PVSK grains and even out of the PVSK layer to interfere with the metal electrode when exposed to thermal energy.[28] This generates defects that detrimentally function as non-radiative recombination sites at the grain boundaries.[29] Also, the randomly oriented PVSK crystallites may result in

Context & Scale

To overcome the barrier of the commercialization of metal halide perovskite solar cells, a simple, cost-effective, and generalized strategy that mitigates the intrinsic thermal instability is strongly needed. Here, caffeine is introduced to simultaneously enhance the efficiency and thermal stability of the solar cells based on various kinds of perovskite materials. The strong interaction between caffeine and Pb^{2+} ions serves as a "molecular lock" that increases the activation energy during film crystallization, delivering a perovskite film with preferred orientation, improved electronic properties, reduced ion migration, and greatly enhanced thermal stability. Ultimately, a champion-stabilized efficiency of 19.8% with 1,300 h thermal stability at 85°C in nitrogen was achieved.

poor charge transport in the vertical direction, a consequence of the fast and uncontrollable growth process of the PVSK film.[30,31]

To date, most reported strategies to realize remarkable thermal stability focused on the device architectures.[32,33] Park and coworkers included atomic layer deposition (ALD) aluminum-doped zinc oxide, which achieved 500 h of thermal stability at 85°C in air.[34] Seo and coworkers utilized a novel fluorene-terminated hole-transporting material realizing 500 h of stability at 85°C in air.[35] Impressed stability has also been shown in architectures that are "hole-conductor free" made by infiltrating porous layers of carbon, ZrO_2, and TiO_2.[36] Studies focus on improving the quality of PVSK layer itself to overcome these demerits.[37,38] Increasing the activation energy for thermal decomposition of the PVSK film is significant to prolong the long-term thermal stability of PVSK solar cells.

On the other hand, many attempts have been made to obtain high-quality PVSK films that mitigate these challenges by utilizing various specific functional groups that can interact with PVSK. Park and coworkers introduced dimethyl sulfoxide (DMSO) with S=O group to retard the crystal growth via the Lewis base-acid adduct method.[39] Han and coworkers introduced [6,6]-phenyl C_{61}-butyric acid methyl ester (PCBM) to eliminate Pb-I defects by forming fullerene-halide radicals.[40] Niu et al. utilized conjugated small molecules with carboxyl and cyano groups to passivate grain boundaries.[41] There are also several studies that incorporated volatile or non-volatile small molecules or polymer additives with similar functional groups to passivate the trap defects and improve the device performance.[42–45] However, it remains difficult to slow down the crystal growth and control the orientated crystals for the purpose of simultaneously boosting the device PCE and long-term stability without sacrificing its electronic properties.[46]

Herein, we introduced a small molecule 1,3,7-trimethylxanthine (Figure 1A), popularly known as caffeine, into the MA-based PVSK. By utilizing the carboxyl groups in the different chemistry environment,[47] caffeine served as a "molecular lock" that interacted strongly with Pb^{2+} ions to slow down the PVSK crystal growth and induced a preferred orientation by increasing the activation energy. The superior crystallinity of the PVSK films with caffeine showed a reduced defect density and better vertical charge transport, achieving a champion PCE as high as 20.25%. In parallel, the excellent film quality suppressed ion migration, and the non-volatile caffeine interacted with the PVSK again during the degradation process to improve the thermal stability of the device. Ultimately, the caffeine-based devices were shown to be thermally stable at 85°C for over 1,300 h.

RESULTS AND DISCUSSION
Effects of Caffeine on the PVSK Film Crystal Growth
Figure 1B shows the Fourier transform infrared spectroscopy (FTIR) spectra of caffeine, pristine $MAPbI_3$, and $MAPbI_3$ with caffeine. The stretching vibrations related to the two C=O bonds stretching in pure caffeine appear at 1,652 cm^{-1} and 1,699 cm^{-1}, respectively.[47] Upon adding caffeine into $MAPbI_3$ film, it is observed that only the C=O stretching with lower frequency (due to the conjugation with C=C bond resulting in the electron delocalization) shifted from 1,652 to 1,657 cm^{-1}, while the vibration mode of C=O at 1,699 cm^{-1} maintains its original value. This indicates the existence of caffeine in the PVSK film after annealing, and caffeine likely formed an adduct with $MAPbI_3$ via the interaction between Pb^{2+} in PVSK and one of the C=O bonds in caffeine.[48] The FTIR spectra of pure PbI_2 and

[1]Department of Materials Science and Engineering and California NanoSystems Institute, University of California Los Angeles, Los Angeles, CA 90095, USA

[2]Institute of Functional Nano & Soft Materials (FUNSOM), Jiangsu Key Laboratory for Carbon-Based Functional Materials & Devices, Soochow University, Suzhou 215123, China

[3]State Key Laboratory on Integrated Optoelectronics, College of Electronic Science and Engineering, Jilin University, Changchun 130012, China

[4]Solargiga Energy Holdings Limited, Hong Kong 999077, China

[5]These authors contributed equally

[6]Present address: College of Chemistry, University of California, Berkeley, Berkeley, CA 94720, USA

[7]Lead Contact

*Correspondence:
zkwang@suda.edu.cn (Z.-K.W.),
yangy@ucla.edu (Y.Y.)
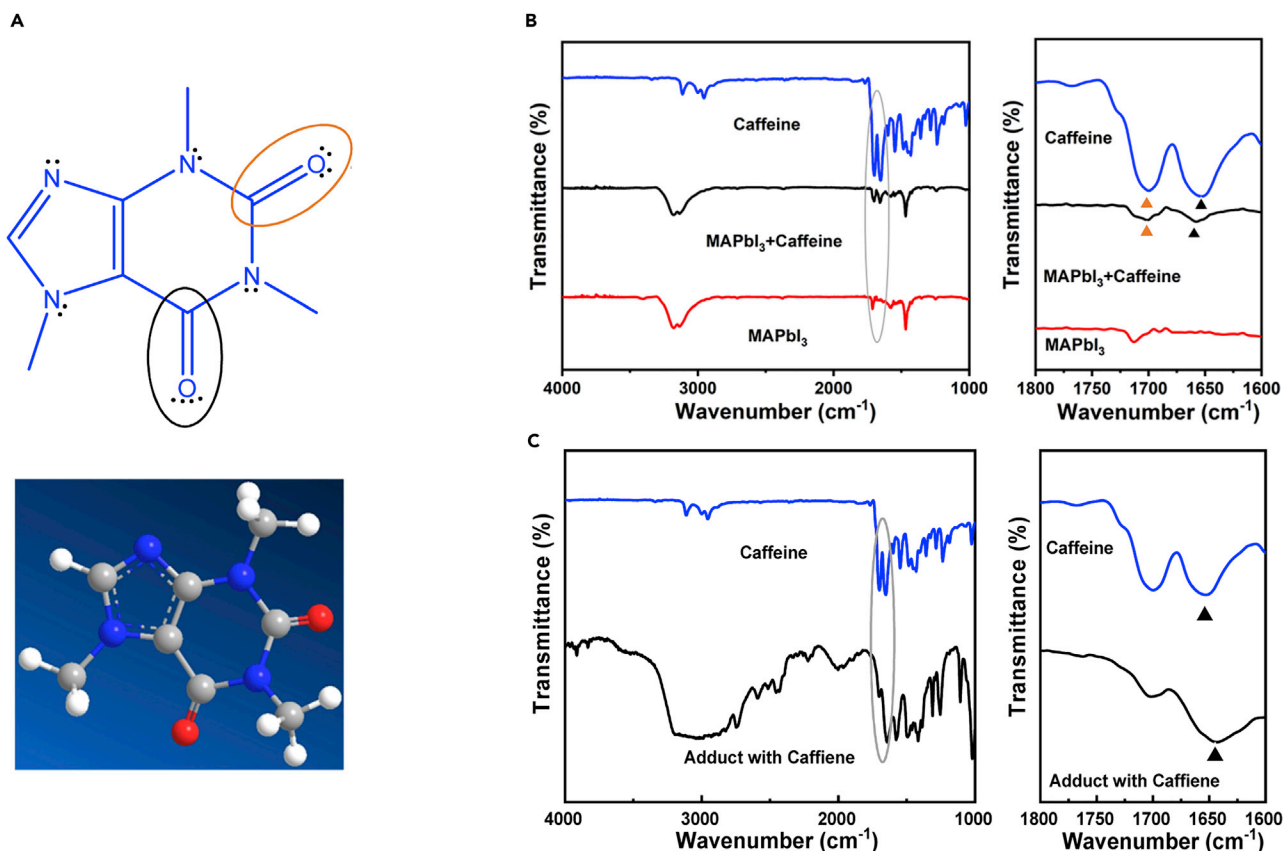https://doi.org/10.1016/j.joule.2019.04.005

Figure 1. Interaction between the Caffeine and Perovskite

(A) Lewis chemical structure and 3D structure of 1,3,7-trimethylxanthine (caffeine).

(B) FTIR spectra and fingerprint regions of pure caffeine, caffeine-PVSK, and the pristine PVSK films. The triangles indicate the stretching vibration peaks of C=O in the two films.

(C) FTIR spectra and fingerprint regions of pure caffeine and PbI_2-MAI-DMSO-caffeine adduct film. The triangles indicate the stretching vibration peaks of C=O in the two films.

PbI_2: caffeine were also measured to further verify that caffeine interacted with the Pb^{2+} to form a strong Lewis acid-base adduct[7] (Figure S1). The shifts of the two characteristic C=O stretches followed the same trend as that of the PVSK case. This interaction was further confirmed by the shift of the Pb 4f orbital in the X-ray photoelectron spectroscopy (XPS) (Figure S2). To study the role of caffeine in PVSK crystal growth, we additionally conducted the FTIR on the PbI_2-MAI-DMSO-caffeine adduct and observed that the same C=O stretching vibration shifted from 1,652 to 1,643 cm^{-1} (Figure 1C). Therefore, this strong interaction of C=O in caffeine with Pb^{2+} ions was expected to serve as a molecular lock to increase the activation energy of nucleation, which retarded the perovskite PVSK crystal growth and improved the crystallinity of the PVSK films with a preferred orientation. More importantly, the residual molecular lock possibly interacted with the amorphized PVSK again upon heating, which can play a crucial role in prohibiting the thermal-induced decomposition.

Figure 2A shows the cross-sectional scanning electron microscopy (SEM) of the caffeine-incorporated PVSK film. Then, we conducted steady-state photoluminescence (PL) and time-resolved photoluminescence (TRPL) decay measurements to study the film quality and charge recombination dynamics, as shown in Figures 2B and 2C, respectively. The PL intensity of the caffeine-incorporated PVSK film was
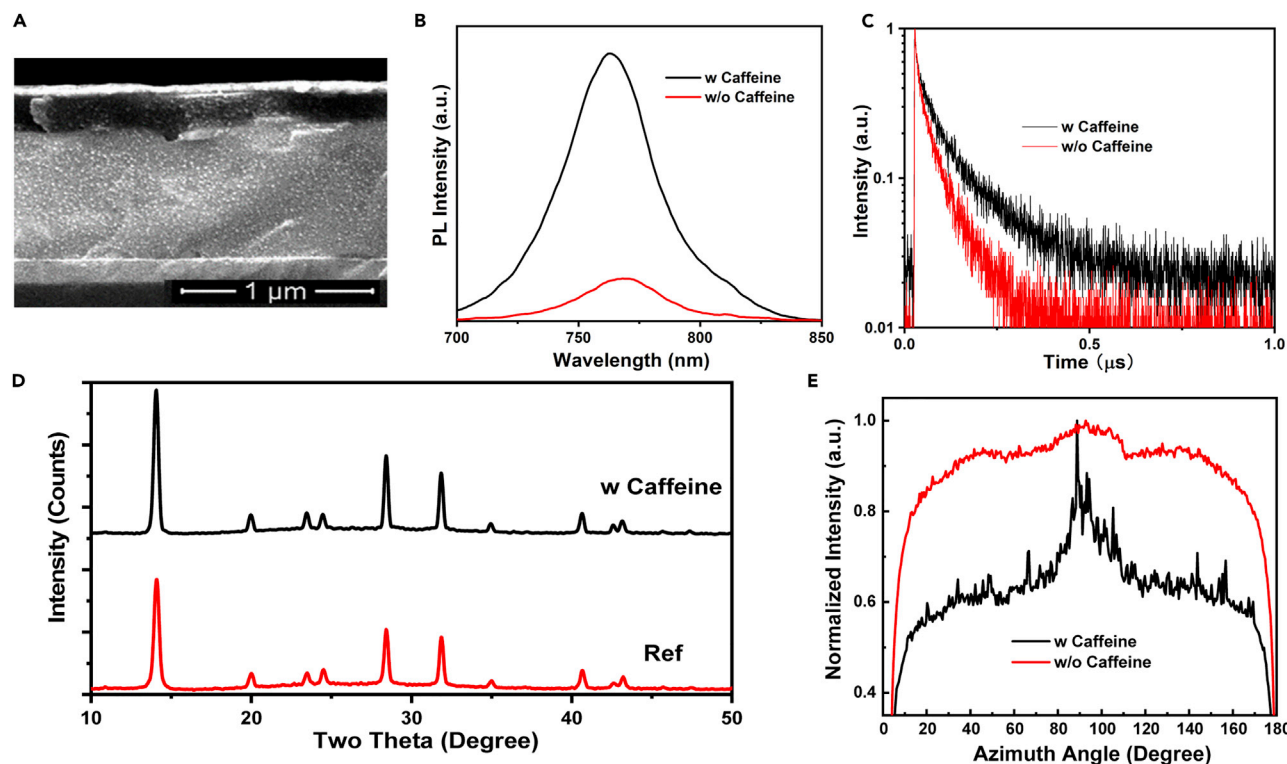
Joule

CellPress

Figure 2. Effects of Caffeine on the PVSK Film Crystal Growth

(A) Cross-sectional SEM of caffeine-containing perovskite film.

(B and C) Photoluminescence (PL) (B) and time-resolved PL spectra (C) of PVSK films without and with caffeine.

(D) X-ray diffraction patterns of as-cast PVSK films with or without caffeine.

(E) Radially integrated intensity plots along (110) crystal plane from the 2D grazing incidence wide-angle X-ray diffraction (GIWAXS) patterns in $MAPbI_3$ and $MAPbI_3$: caffeine films.

enhanced by six times compared to that of the pristine PVSK film. Simultaneously, the peak position was blue-shifted from 770 to 763 nm, which further confirmed that the number of trap states was reduced upon the addition of caffeine (Figure S3). Bi-exponential rate law model was employed to fit the PL decay. Both the pristine $MAPbI_3$ and the caffeine-incorporated $MAPbI_3$ films showed relatively faster decay time (τ_1) and relatively slower decay time (τ_2).[49] The faster decay is likely related to non-radiative recombination induced by charge-trapping defect states. On the other hand, τ_2 represents the bi-molecular recombination in the bulk film. With the addition of caffeine, the fraction of the fast decay phase lifetime decreased from 57.8% to 41.9%, and the lifetime increased from 7.4 to 21.98 ns. Notably, the slow decay phase lifetime enhanced from 51.9 to 114.3 ns. These results further demonstrate the lower trap density and better electronic properties of the caffeine-incorporated PVSK film.

To examine the crystal structure, we conducted thin-layer X-ray diffraction (XRD) measurements for the PVSK films deposited on indium tin oxide (ITO) substrate (Figure 2D). The diffraction peak at 12.5°, assigned to the (001) planes of the hexagonal PbI_2, was not detected for both the $MAPbI_3$ and $MAPbI_3$: caffeine films. Both films showed the same tetragonal PVSK phase with the dominant (110) lattice reflection at 13.9°, which is the preferred orientation for the PVSK films. The ratio of the (110) peak intensity at 13.9° to the (222) peak intensity at 31.8° increased from 2.00 to 2.43 upon incorporation of caffeine. This suggests that the (110) grains
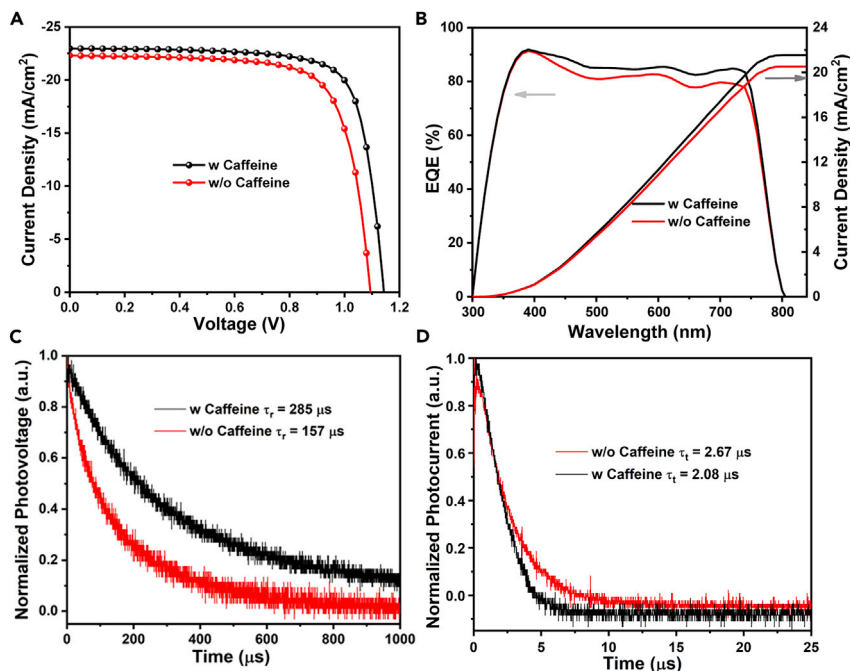
Figure 3. Enhanced Photovoltaic Performances and TPC and TPV Analysis

(A) *J-V* curves of the champion PSC of pristine PVSK and caffeine-containing PVSK in reverse scan direction.

(B) EQE spectra and integrated current densities from the EQE spectra of PVSK devices with or without adding caffeine.

(C and D) Normalized transient photovoltage (TPV) decay (C) and normalized transient photocurrent (TPC) decay (D) in MAPbI$_3$ and MAPbI$_3$: caffeine-based perovskite solar cells.

grew faster by consuming the randomly oriented neighboring crystals. We calculated the crystallite size using the Scherrer's equation and by taking the full-width half-maximum (FWHM) of the (110) peak. At the optimized ratio of caffeine added, the crystallite size increased from 37.97 to 55.99 nm, consistent with the surface SEM images of the PVSK films (Figure S4). Obviously, the caffeine-incorporated PVSK showed an overall crystallinity enhancement, which was further confirmed by two-dimensional (2D) grazing incidence wide-angle X-ray diffraction (GIWAXS) analysis. Figure 2E shows the normalized azimuth angle plots along the (110) plane of pure MAPbI$_3$ and caffeine-incorporated MAPbI$_3$ (1 wt %) films, which were integrated from the 2D GIWAXS patterns (Figure S5). At the azimuth angle of 90°, the caffeine-incorporated PVSK film shows a very sharp peak compared with the pristine PVSK film. The narrower FWHM suggests that the incorporation of caffeine assisted the growth of the PVSK grains along the in-plane direction, which would enhance the charge transport of the device.[49]

Device Performance and TPC and TPV Analysis

The photovoltaic devices were fabricated with a n-i-p planar structure. ITO was used as the anode. Tin oxide nanoparticles[50] were employed as the electron-transporting layer. Pure MAPbI$_3$ and MAPbI$_3$: caffeine at various concentrations were employed as the active layer. Poly[bis(4-phenyl)(2,4,6-trimethylphenyl)amine] (PTAA) doped with 4-isopropyl-4'-methyldiphenyliodonium tetrakis (pentafluorophenyl) borate (TPFB)[51] was employed as the hole-transporting layer (HTL). Silver (Ag) was used as the cathode. Figure 3A shows the *J-V* curves of the champion devices based on

Table 1. Average and the Best Device Data Based on MAPbI$_3$ with Various Concentrations of Caffeine

Caffeine Concentration (wt %)	V_{OC} (V)	J_{sc} (mA cm^{-2})	Calculated J_{sc} (mA cm^{-2})	FF (%)	PCE (%)	
					Average	Best
0	1.071 ± 0.01	21.78 ± 0.31	20.58	72.52 ± 1.32	16.92 ± 0.40	17.59
0.5	1.107 ± 0.01	21.77 ± 0.54	20.89	73.60 ± 1.48	17.74 ± 0.17	17.98
1	1.134 ± 0.01	22.77 ± 0.30	21.53	76.90 ± 1.13	19.87 ± 0.22	20.25
2	1.132 ± 0.01	22.16 ± 0.26	21.24	73.21 ± 1.22	18.40 ± 0.37	18.82

pure MAPbI$_3$ and MAPbI$_3$: caffeine measured under reverse scanning, as illuminated by an AM 1.5G solar simulator with an intensity of 100 mW cm^{-2}. The ratio of caffeine added was varied from 0 to 2 wt %. With increasing amounts of caffeine from 0 (reference) to 1 wt %, the open-circuit voltage (V_{OC}), short-circuit current (J_{sc}), fill factor (FF), and reproducibility were systematically enhanced (Figure S6). The highest PCE achieved for the pure MAPbI$_3$ devices was 17.59% (V_{oc}: 1.074 V, J_{sc}: 22.29 mA/cm^2, and FF: 73.46%). In contrast, a PCE of 20.25% (V_{oc}: 1.143 V, J_{sc}: 22.97 mA/cm^2, and FF: 77.13%) was achieved for the optimized devices with 1 wt % caffeine. The enhanced V_{oc} and FF may be associated with decreased non-radiative recombination and crystal defects owing to the passivation effect induced by the incorporation of caffeine, consistent with the PL and TRPL results. The J_{sc} was also enhanced from 22.29 to 22.97 mA/cm^2, which was confirmed by the external quantum efficiency (EQE) spectra of devices based on pure MAPbI$_3$ and MAPbI$_3$: caffeine (Figure 3B). The calculated J_{sc} values obtained from the integration of the EQE spectra were close to the measured values with the AM 1.5G reference spectrum (average mismatch is below 5%, Table 1). The quantum efficiency enhancement in the long wavelength region was consistent with the ultraviolet-visible (UV-vis) absorption spectra (Figure S7). The absorption enhancement may have resulted from the larger crystal size and better crystallinity of the caffeine-incorporated devices, which has been proven to enhance the light-harvesting efficiency caused by enhanced light scattering. The steady-state PCEs of the best-performing devices were 17.04% and 19.76% for the devices without and with caffeine, respectively (Figure S8). J-V hysteresis between the reverse and forward scan directions was also decreased with the addition of caffeine. The hysteresis index $\left(\frac{PCE_{Reverse} - PCE_{Forward}}{PCE_{Reverse}} \right)$ decreased from 0.157 to 0.097 upon addition of 1 wt % caffeine (Figure S9; Table S1). To demonstrate the universality of caffeine, we examined the device performances of the devices based on mixed A-site cations and mixed halide PVSK (CsFAMAPbI$_x$Br$_{3-x}$). The J-V curves under both reverse and forward scan directions and the steady-state output efficiency are shown in Figure S10 and Table S2. The PVSK solar cells with caffeine showed enhanced photovoltaic performance compared to the reference, which indicates this approach could be effective and universal.

To gain further insight into the performance enhancement resulting from the use of caffeine, we characterized the charge-transfer kinetics and charge recombination in the pure MAPbI$_3$ and MAPbI$_3$: caffeine solar cells.[9] We used transient photovoltage decay (TPV) under the open-circuit condition to characterize the solar cells and found that the charge-recombination lifetime (τ_r) of the MAPbI$_3$: caffeine-based device was substantially longer than that of the device based on pure MAPbI$_3$ (285 μs versus 157 μs) (Figure 3C), consistent with the slowed charge recombination in the MAPbI$_3$: caffeine film, as concluded from the TRPL measurement. This indicates a lower defect concentration and hence superior electronic quality in the

Joule

CellPress

caffeine-incorporated PVSK bulk film, consistent with the higher V_{oc} of the corresponding devices. Meanwhile, transient photocurrent decay (TPC) under the short-circuit condition was conducted to investigate the influence of caffeine on the charge transfer in the devices. Although the addition of caffeine did not affect the band structure of the PVSK (Figure S11), the charge transfer lifetime (τ_t) of the caffeine-containing PVSK decreased from 2.67 to 2.08 µs. The enhanced charge transfer might have resulted from the reduced interfacial defects and the better crystal orientation of the MAPbI$_3$: caffeine films.

Thermal Stability and TGA Analysis

To prove the molecular locking effect of caffeine on the corresponding PVSK devices during the thermal degradation process, we conducted a continuous thermal stress stability test for the devices based on bare MAPbI$_3$ and MAPbI$_3$: caffeine at 85°C in a nitrogen atmosphere. The device with caffeine showed excellent thermal stability, preserving 86% of its original PCE after 1,300 h. The represented *J-V* curves before and after being subjected to the thermal stability test are shown in Figures S12, S18, and S19. The controlled device only retained 60% of its original PCE after 175 h, which may be due to ion migration, poor crystal quality, and phase instability of bare MAPbI$_3$ at high temperatures. Furthermore, to evaluate the operational stability, all the devices were encapsulated under a nitrogen atmosphere and exposed to continuous illumination (90 $\pm$ 10 mW, without UV filter) under open-circuit conditions (Figure S13). Caffeine can also effectively enhance the operational stability of the PVSK solar cell. To understand the mechanism of the enhanced thermal stability of the caffeine-incorporated devices in the context of ion migration and phase decomposition, we first conducted XRD analysis on the devices after the thermal stability test (Figure 4B). For the reference device, there was a strong peak at 12.5°, attributed to the (001) planes of hexagonal PbI$_2$. The extremely weak diffraction at 13.9° suggests a complete degradation of the PVSK crystal. Not surprisingly, there was a relatively strong diffraction signal at 38.5°, assigned to the (003) plane of PbI$_2$. Although there was a peak at 12.5° in the target device, the (110) plane signal was still strong. The superior crystallinity of the caffeine-incorporated PVSK might have resulted in the suppression of ion migration during heating. Thermogravimetric analysis (TGA) on caffeine and the adduct powders was conducted to analyze the phase stability and thermal properties of caffeine and the intermediate adduct phase. Figures 4C and 4D indicate the weight loss and heat flow of the powders, respectively, based on caffeine, pure PVSK, and caffeine-incorporated PVSK. Caffeine decomposed completely at around 285°C, demonstrating its superior thermal stability at temperatures below 200°C (Figure S14). From Figure 4C, there are three main steps of the weight loss at around 70°C, 340°C, and 460°C for the pure PVSK powders. These three steps are correlated with the sublimation of DMSO, MAI, and PbI$_2$, respectively.[45] For the caffeine-containing PVSK adduct powders, the sublimation temperature of MAI and PbI$_2$ were higher than that of the bare PVSK powders, which indicates that more energy is required to break the interaction between caffeine and the PVSK precursors. This is further confirmed by the heat flow diagrams as shown in Figure 4D. The strong interaction formed by the caffeine molecular lock may increase the activation energy for the decomposition upon heating.

Microstructure Analysis via Cross-Sectional STEM and *In Situ* HRTEM

To further investigate the role of caffeine in suppressing ion migration and thermal decomposition, microstructure analysis was carried out. We first conducted cross-sectional scanning transmission electron microscopy (STEM) and energy-dispersive X-ray (EDX) spectroscopy analysis (Figure 5). The samples were directly collected
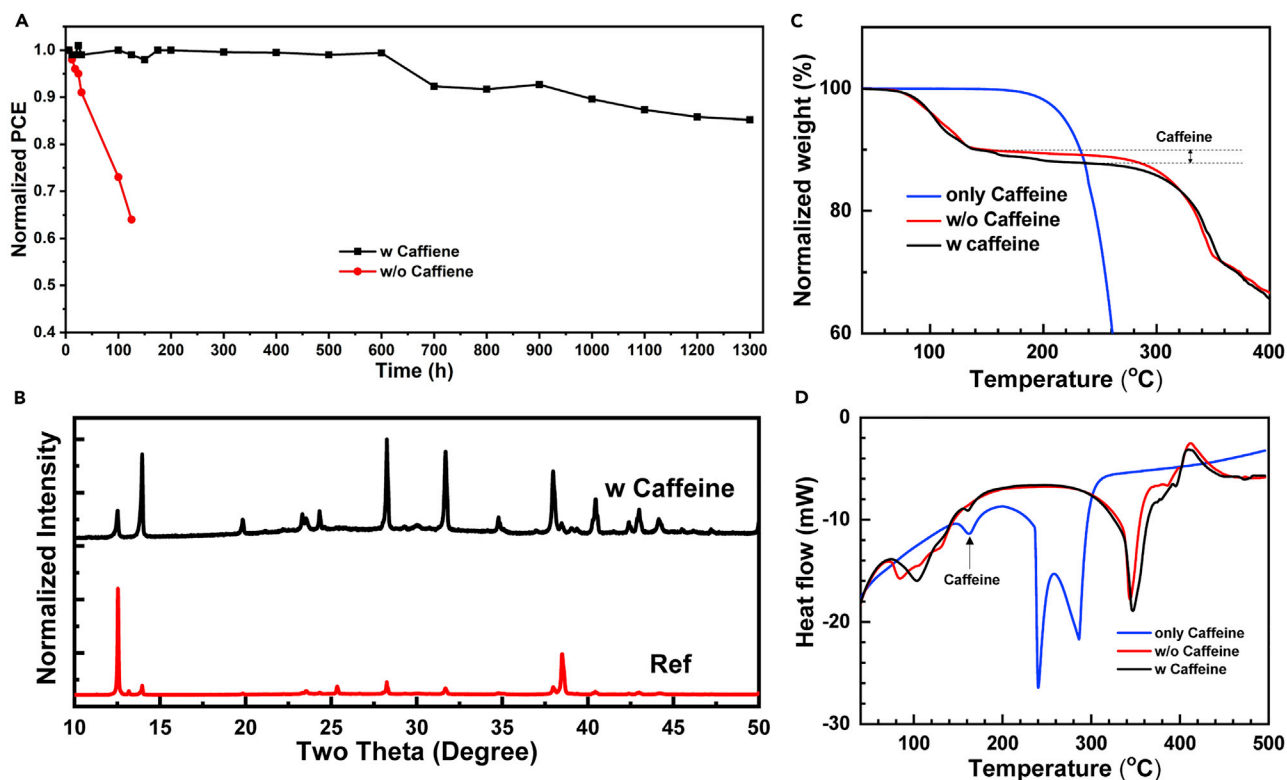
Joule

CellPress

Figure 4. Enhanced Thermal Stability

(A) Devices thermal stability upon 85°C continuous annealing in nitrogen box.

(B) XRD patterns of aged device based on pure $MAPbI_3$ and $MAPbI_3$ with caffeine.

(C and D) Thermogravimetric analysis (TGA) of weight loss (C) and heat flow (D) of pristine caffeine, $MAI\text{-}PbI_2\text{-}DMSO$ adduct powder, and $MAI\text{-}PbI_2\text{-}DMSO$-caffeine adduct powder.

from the devices after the 1,300-h thermal stability test via focused ion beam (FIB). Figure S15 shows the EDX mapping of selective regions on both the control and target devices. The spatial distribution of the Pb and I elements determined the PVSK active layer region. The Ag electrode was above the active layer, separated by the PTAA HTL. For the control sample, there were significant Ag signals (Ag clusters) with a similar intensity as that in the electrode region detected at the interface between the HTL and the active layer region. It is likely that the Ag diffused through the whole PVSK region, as confirmed by the observation that the Ag signals were detected even in the ITO electrode region. More importantly, the iodine signals were clearly detected in the Ag electrode region. Iodine could accumulate at the electrode and interface. It easily reacted with Ag to form AgI, which will negatively impact the device performance. In contrast, there is no obvious indication of such similar ion migration in the caffeine-incorporated PVSK device. To further confirm the result quantitively, line-scanning profiles were also measured. As shown in Figure 5G, the thickness of the Ag electrode was 50 nm, two sharp peaks at both the electrode and interface were observed, and the Ag signal was detected almost throughout the entire device. However, the thickness of the Ag electrode in the caffeine-incorporated PVSK device maintained its original value of 100 nm. More importantly, a sharp iodine peak was detected in the electrode region of the control device, in agreement with the previous conclusion. Hence, from the STEM results, the suppression of ion migration in the caffeine-containing films ensured the high thermal resistance of the devices. We also conducted real-time high-resolution
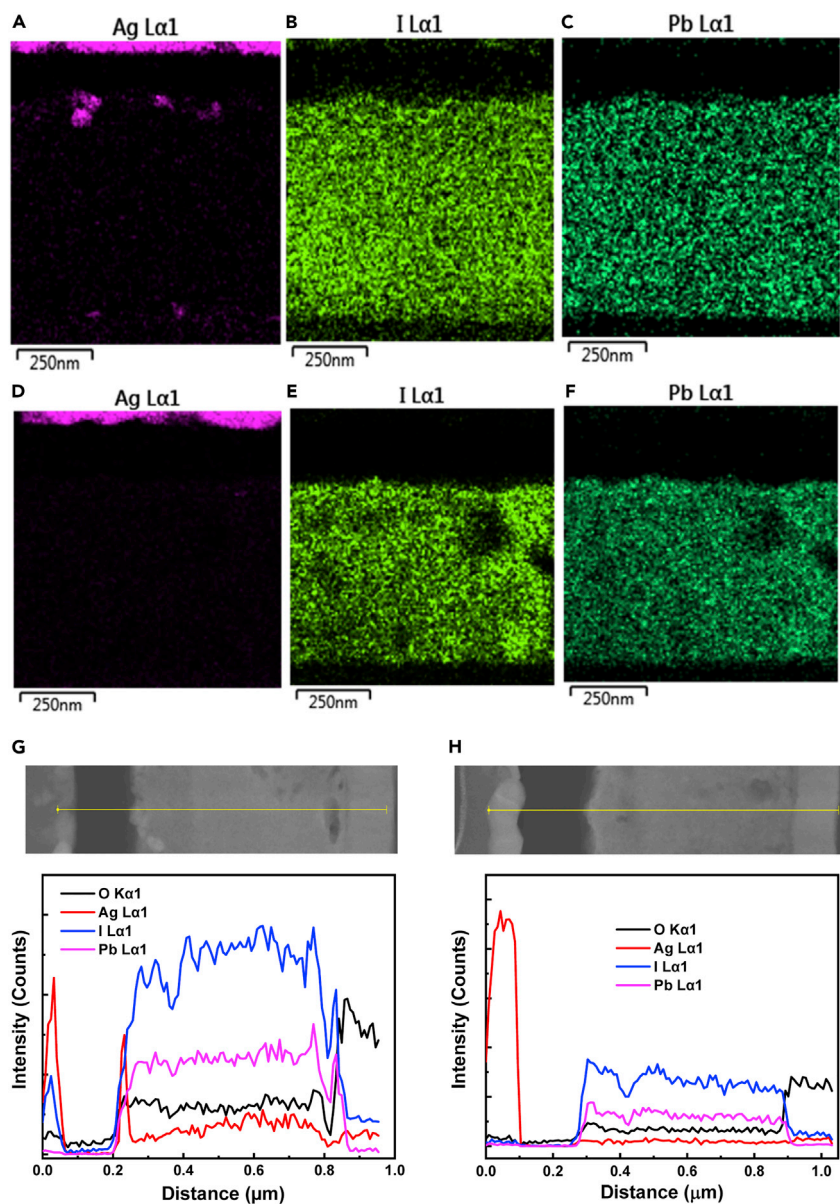
Joule

CellPress

Figure 5. Suppressed Ion Migration

(A–F) Energy-dispersive X-ray spectra (EDX) mapping of the aged pure PVSK device (A) Ag, (B) I, and (C) Pb, and the aged caffeine-containing PVSK device (D) Ag, (E) I, and (F) Pb.

(G and H) EDX line scans of (G) aged pure PVSK device and (H) aged caffeine-containing PVSK device.

transmission electron spectroscopy (HRTEM) to study the effect of caffeine on the phase transformation of the PVSK. The electron beam (E-beam) of the HRTEM instrument was utilized as the source of the thermal energy. Figures 6A–6D show the HRTEM images and the corresponding fast Fourier transforms (FFTs) of the diffraction patterns of both the caffeine-incorporated and pristine PVSKs. $MAPbI_3$ layers with various crystallographic orientations were observed in both samples. The representative spot diffractions (yellow circles) with an interplanar spacing of 3.1 Å, which are well matched with the (110) diffraction of $MAPbI_3$, are shown in Figures 6B and 6D. After exposure to the E-beam for 5 min 30 s, the environmental temperature

Joule

CellPress
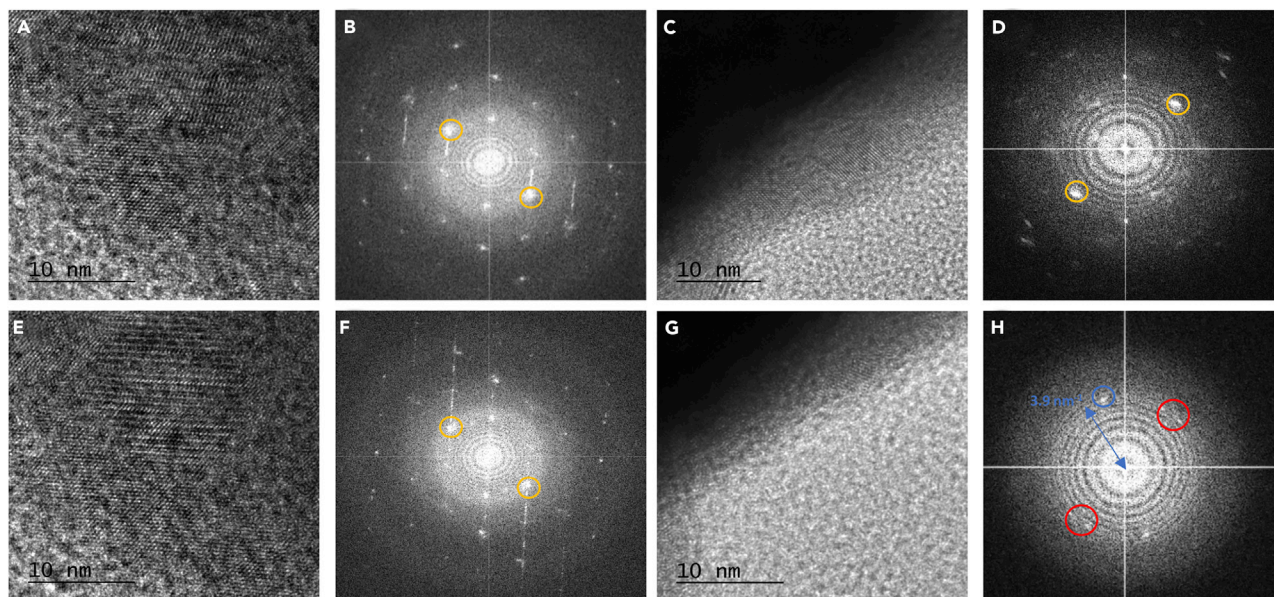
Figure 6. Formation of Molecular Lock

High resolution transmittance electron microscopy (HRTEM) of (A) fresh caffeine containing PVSK, (C) fresh pure PVSK, (E) aged (5 min 30 s) caffeine containing PVSK, and (G) aged (5 min 30 s) pure PVSK. Corresponding fast Fourier transforms (FFTs) of (B) fresh caffeine containing PVSK, (D) fresh pure PVSK, (F) aged (5 min 30 s) caffeine containing PVSK, and (H) aged (5 min 30 s) pure PVSK.

of the samples was elevated to around 135°C.[52] Figures 6E–6H present the HRTEM images and the corresponding FFTs of the diffraction patterns of the aged caffeine-incorporated and pristine PVSKs. Although the intensity of the (110) diffraction spots of the caffeine-incorporated PVSK became weak, no new diffraction peaks appeared. Notably, a critical alteration of the $MAPbI_3$ layer was observed in the control sample with the (110) diffraction spots observed to split (red circle). On the other hand, there was a new broad ring that appeared in the FFT at $3.9 \, nm^{-1}$, and new diffraction spots were observed at the same place. These morphological characteristics suggest that some crystallized PVSK phase had been transferred to the amorphized phase with precipitated trigonal PbI_2 grains at this region, which agrees with a previous study that the thermal degradation of PVSK is often considered as the reverse process of the PVSK film growth.[53] We also conducted *in situ* TEM measurement on the other regions of the films, and the results followed a similar trend as described previously (Figures S16 and S17). From these results, we speculate that the existence of the caffeine additive serves as a molecular lock to interact with the amorphized PVSK phase again to increase the decomposition activation energy of the PVSK, which locks the amorphized phase of the PVSK, thereby preventing the degradation of the PVSK when exposed to high temperatures.

Conclusions

In conclusion, we employed caffeine, a conjugated Lewis base with two carboxyl groups, to serve as a molecular lock on PVSK. The strong interaction between caffeine and the Pb^{2+} ions increased the growth activation energy of the PVSK film, which facilitated the growth of high-quality films that showed preferred orientation and superior electronic properties. Consequently, a PCE as high as 20.25% was achieved for the champion device. In the meantime, the superior film quality suppressed the migration of ions. Also, the residual conjugated molecular lock effectively prevented any form of thermal degradation (the reverse of the PVSK synthesis

process), which realized PVSK: caffeine-based solar cells that were thermally stable for over 1,300 h at 85°C.

EXPERIMENTAL PROCEDURES

Materials

Unless stated otherwise, solvents and chemicals were obtained commercially and used without further purification. N, N-dimethylformamide (DMF), DMSO, chlorobenzene (CB), caffeine, toluene, water, and Ag were obtained from Sigma-Aldrich Inc. TPFB and PbI_2 were obtained from TCI Inc. MAI was obtained from One Materials. PTAA was obtained from Xi'an Polymer Light Technology Corp and Sigma-Aldrich Inc (Lot# MKCD5161). Tin oxide (SnO_2) nanoparticle was obtained from Alfa-Aesar Inc.

Device Fabrication

PVSK solar cells were fabricated with the following structures: indium tin oxide (ITO), SnO_2, $MAPbI_3$, PTAA, and Ag. The ITO glass was pre-cleaned in an ultrasonic bath of acetone and isopropanol, and treated in ultraviolet-ozone for 20 min. A thin layer (~30 nm) of SnO_2 was spin-coated onto the ITO glass and baked at 150°C for 30 min. SnO_2 was diluted in water (1.67 mg mL^{-1}). After cooling at room temperature, the glass, ITO, and SnO_2 substrates were transferred into a nitrogen glove box. PVSK solution was prepared by dissolving 159 mg MAI and 461 mg PbI_2 and 71 μL DMSO in 600 μL DMF. For the optimized caffeine containing PVSK, 6 mg caffeine was added into the solution. The PVSK solution was spin-coated on the substrate at 2,500 rpm for 25 s, to which 0.1 mL of CB was dropped after 10 s. The spin-coated film was heat treated at 65°C for 1 min followed by 100°C for 20 min. The PTAA solution (30 mg mL^{-1}, in CB with 10% TPFB) was spun onto the PVSK film as a hole conductor. The devices were completed by evaporating 100 nm Ag in a vacuum chamber (base pressure, 5×10^{-4} Pa).

Synthesis of Adduct Powders

For $MAI \cdot PbI_2 \cdot DMSO$ and $MAI \cdot PbI_2 \cdot DMSO \cdot$ caffeine adducts, 1 mmol of PbI_2, MAI, and DMSO with or without 6 mg caffeine were dissolved in 600 μL of DMF, to which 10 mL of diethyl ether was added to precipitate the corresponding adduct. The precipitates were collected and dried under vacuum.

Device Characterization

J-V characteristics of photovoltaic cells were taken using a Keithley 2400 source measure unit under a simulated AM 1.5G spectrum, with an Oriel 9600 solar simulator. Typically, the devices were measured in reverse scan (1.2 V → 0 V, step 0.02 V, 100 mV/s) and forward scan (0 V → 1.2 V, step 0.02 V, 100 mV/s). All the devices were measured without pre-conditioning such as light-soaking and applied bias voltage. Steady-state power conversion efficiency was calculated by measuring stabilized photocurrent density under constant bias voltage. EQEs were measured using an integrated system (Enlitech, Taiwan) and a lock-in amplifier with a current preamplifier under short-circuit conditions. For TPV and current (TPC) measurements, a white light bias was generated from an array of diodes (Molex 180081-4320) to simulate 0.5 sun bias light working condition. A pulsed red dye laser (Rhodamine 6G, 590 nm) pumped by a nitrogen laser (LSI VSL-337ND-S) was used as the perturbation source, with a pulse width of 4 ns and a repetition frequency of 10 Hz. The intensity of the perturbation laser pulse was controlled to maintain the amplitude of transient VOC below 5 mV so that the perturbation assumption of excitation light holds. The voltages under open circuit and currents under

Joule

CellPress

short-circuit conditions were measured over a 1 MΩ and a 50 Ω resistor and were re-corded on a digital oscilloscope (Tektronix DPO 4104B).

Materials Characterization

UV-vis absorption spectra of the PVSK films were obtained using a U-4100 spectro-photometer (Hitachi) equipped with integrating sphere in which monochromatic light was incident to the substrate side. XRD patterns of the films were recorded by X-ray diffractometer (PANalytical) with Cu kα radiation at a scan rate of 4°/min. Surface and cross-sectional microscopic images of the films and devices were ac-quired by SEM (Nova Nano 230). ∼1-nm-thick gold was sputtered on cross-sectional samples to enhance the conductivity. Transmission Fourier transform infrared (FTIR) spectroscopic analysis was performed using FT/IR-6100 (Jasco). The chamber was purged with nitrogen gas during the measurement. Steady-state PL measurement was carried out using Horiba Jobin Yvon system in which a 640 nm monochromatic laser was used as an excitation fluorescence source. Time-resolved PL decay profiles of the PVSK films were investigated by a Picoharp 300 with time-correlated single-photon counting capabilities. A 640 nm monochromatic pulsed laser with a repeti-tion frequency of 100 kHz was generated from a picosecond laser diode head (PLD 800B, PicoQuant). The energy density of the excitation light was controlled to be ∼1.4 nJ/cm^2.

GIWAXS test was performed at the BL14B1 beamline of China Shanghai Synchrotron Radiation Facility (SSRF). 2D GIWAXS patterns were obtained by a MarCCD 225 de-tector mounted vertically at around 256.401 mm from the sample with an exposure time of 50 s at a grazing incidence angle of 0.15°. The x axis of GIWAXS patterns were represented by the diffraction vector with $q = 4\pi\sin(\theta)/\lambda$, where θ is half of the diffraction angle and λ is the wavelength of incident X-ray. XPS measurements were carried out on an XPS AXIS Ultra DLD (Kratos Analytical). An Al Kα (1,486.6 eV) X-ray was used as the excitation source. UPS measurements were car-ried out to determine the work function and the position of valence band maximum of materials. A He discharge lamp, emitting ultraviolet energy at 21.2 eV, was used for excitation. All UPS measurements were performed using standard procedures with a −9 V bias applied between the samples and detectors. Clean gold was used as a reference. High angle annular dark field scanning transmission electron mi-croscopy (HAADF STEM) images, EDS maps, and line-scan profiles were taken on a FEI Titan STEM operated at 300 kV. The device glass, ITO, SnO$_2$, PVSK, PTAA, and Ag was used for the TEM sample. The focused ion beam technique was used for cross-TEM sample preparation. HRTEM analysis was performed by Titan (FEI). The PVSK film was scratched off from the substrate and dispersed in toluene by sonicat-ion for 10 min, which was dropped on a copper grid. Accelerating voltage of 300 kV was used for the measurement. TGA was conducted using SDT Q600 (TA instru-ments) under dry air with a heating rate of 10°C/min.

SUPPLEMENTAL INFORMATION

Supplemental Information can be found online at https://doi.org/10.1016/j.joule.2019.04.005.

ACKNOWLEDGMENTS

Joule

CellPress

AUTHOR CONTRIBUTIONS

DECLARATION OF INTERESTS

The authors declare no competing interests.

REFERENCES

1. Chiba, T., Hayashi, Y., Ebe, H., Hoshi, K., Sato, J., Sato, S., Pu, Y.-J., Ohisa, S., and Kido, J. (2018). Anion-exchange red perovskite quantum dots with ammonium iodine salts for highly efficient light-emitting devices. Nat. Photon. *12*, 681–687.

2. Liu, M., Johnston, M.B., and Snaith, H.J. (2013). Efficient planar heterojunction perovskite solar cells by vapour deposition many different photovoltaic technologies are being developed for large-scale solar energy conversion. Nature *501*, 395–398.

3. Cho, H., Jeong, S.H., Park, M.H., Kim, Y.H., Wolf, C., Lee, C.L., Heo, J.H., Sadhanala, A., Myoung, N.S., Yoo, S., et al. (2015). Overcoming the electroluminescence efficiency limitations of perovskite light-emitting diodes. Science *350*, 1222–1225.

4. Xue, J., Zhang, Z., Zheng, F., Xu, Q., Xu, J., Zou, G., Li, L., and Zhu, J.J. (2017). Efficient solid-state electrochemiluminescence from high-quality perovskite quantum dot films. Anal. Chem. *89*, 8212–8216.

5. Wei, H., Desantis, D., Wei, W., Deng, Y., Guo, D., Savenije, T.J., Cao, L., and Huang, J. (2017). Dopant compensation in alloyed CH3NH3PbBr3-xClxperovskite single crystals for gamma-ray spectroscopy. Nat. Mater. *16*, 826–833.

6. Kim, Y.C., Kim, K.H., Son, D.Y., Jeong, D.N., Seo, J.Y., Choi, Y.S., Han, I.T., Lee, S.Y., and Park, N.G. (2017). Printable organometallic perovskite enables large-area, low-dose X-ray imaging. Nature *550*, 87–91.

7. Bi, D., Yi, C., Luo, J., Décoppet, J.-D., Zhang, F., Zakeeruddin, S.M., Li, X., Hagfeldt, A., and Grätzel, M. (2016). Polymer-templated nucleation and crystal growth of perovskite films for solar cells with efficiency greater than 21%. Nat. Energy *1*, 16142.

8. Deng, Y., Zheng, X., Bai, Y., Wang, Q., Zhao, J., and Huang, J. (2018). Surfactant-controlled ink drying enables high-speed deposition of perovskite films for efficient photovoltaic modules. Nat. Energy *3*, 560–566.

9. Tan, H., Jain, A., Voznyy, O., Lan, X., García de Arquer, F.P.G., Fan, J.Z., Quintero-Bermudez, R., Yuan, M., Zhang, B., Zhao, Y., et al. (2017). Efficient and stable solution-processed planar perovskite solar cells via contact passivation. Science *355*, 722–726.

10. Yang, W.S., Noh, J.H., Jeon, N.J., Kim, Y.C., Ryu, S., Seo, J., and Seok, S.I. (2015). SOLAR CELLS. High-performance photovoltaic perovskite layers fabricated through intramolecular exchange. Science *348*, 1234–1237.

11. Burschka, J., Pellet, N., Moon, S.J., Humphry-Baker, R., Gao, P., Nazeeruddin, M.K., and Grätzel, M. (2013). Sequential deposition as a route to high-performance perovskite-sensitized solar cells. Nature *499*, 316–319.

12. Kojima, A., Teshima, K., Shirai, Y., and Miyasaka, T. (2009). Organometal halide perovskites as visible-light sensitizers for photovoltaic cells. J. Am. Chem. Soc. *131*, 6050–6051.

13. National Renewable Energy Laboratory. Photovoltaic research. https://www.nrel.gov/pv/assets/pdfs/pv-efficiencies-07-17-2018.pdf.

14. Yang, W.S., Park, B.W., Jung, E.H., Jeon, N.J., Kim, Y.C., Lee, D.U., Shin, S.S., Seo, J., Kim, E.K., Noh, J.H., et al. (2017). Iodide management in formamidinium-lead-halide-based perovskite layers for efficient solar cells. Science *356*, 1376–1379.

15. Im, J.-H., Lee, C.-R., Lee, J.-W., Park, S.-W., and Park, N.-G. (2011). 6.5% efficient perovskite quantum-dot-sensitized solar cell. Nanoscale *3*, 4088–4093.

16. You, J., Meng, L., Song, T.B., Guo, T.F., Yang, Y.M., Chang, W.H., Hong, Z., Chen, H., Zhou, H., Chen, Q., et al. (2016). Improved air stability of perovskite solar cells via solution-processed metal oxide transport layers. Nat. Nanotechnol. *11*, 75–81.

17. Divitini, G., Cacovich, S., Matteocci, F., Cinà, L., Di Carlo, A., and Ducati, C. (2016). In situ observation of heat-induced degradation of perovskite solar cells. Nat. Energy *1*, 15012.

18. Zheng, X., Chen, B., Dai, J., Fang, Y., Bai, Y., Lin, Y., Wei, H., Zeng, X.C., and Huang, J. (2017). Defect passivation in hybrid perovskite solar cells using quaternary ammonium halide anions and cations. Nat. Energy *2*, 17102.

19. Aristidou, N., Sanchez-Molina, I., Chotchuangchutchaval, T., Brown, M., Martinez, L., Rath, T., and Haque, S.A. (2015). The role of oxygen in the degradation of methylammonium lead trihalide perovskite

Joule

CellPress

photoactive layers. Angew. Chem. Int. Ed. *54*, 8208–8212.

20. Zhang, C.C., Li, M., Wang, Z.K., Jiang, Y.R., Liu, H.R., Yang, Y.G., Gao, X.Y., and Ma, H. (2017). Passivated perovskite crystallization and stability in organic-inorganic halide solar cells by doping a donor polymer. J. Mater. Chem. A *5*, 2572–2579.

21. Li, M., Wang, Z.K., Kang, T., Yang, Y., Gao, X., Hsu, C.S., Li, Y., and Liao, L.S. (2018). Graphdiyne-modified cross-linkable fullerene as an efficient electron-transporting layer in organometal halide perovskite solar cells. Nano Energy *43*, 47–54.

22. Xue, J., Lee, J.-W., Dai, Z., Wang, R., Nuryyeva, S., Liao, M.E., Chang, S.-Y., Meng, L., Meng, D., Sun, P., et al. (2018). Surface ligand management for stable FAPbI3 perovskite quantum dot solar cells. Joule *2*, 1866–1878.

23. Swarnkar, A., Marshall, A.R., Sanehira, E.M., Chernomordik, B.D., Moore, D.T., Christians, J.A., Chakrabarti, T., and Luther, J.M. (2016). Quantum dot-induced phase stabilization of α-CsPbI3 perovskite for high-efficiency photovoltaics. Science *354*, 92–95.

24. Chen, Q., De Marco, N., Yang, Y., Song, T.-B., Chen, C.C., Zhao, H., Hong, Z., Zhou, H., and Yang, Y. (2015). Under the spotlight: the organic-inorganic hybrid halide perovskite for optoelectronic applications. Nano Today *10*, 355–396.

25. Berhe, T.A., Su, W.-N., Chen, C.-H., Pan, C.-J., Cheng, J.-H., Chen, H.-M., Tsai, M.-C., Chen, L.-Y., Dubale, A.A., and Hwang, B.-J. (2016). Organometal halide perovskite solar cells: degradation and stability. Energy Environ. Sci. *9*, 323–356.

26. Conings, B., Drijkoningen, J., Gauquelin, N., Babayigit, A., D'Haen, J., D'Olieslaeger, L., Ethirajan, A., Verbeeck, J., Manca, J., Mosconi, E., et al. (2015). Intrinsic thermal instability of methylammonium lead trihalide perovskite. Adv. Energy Mater. *5*, 1500477.

27. Yang, Y., and You, J. (2017). Make perovskite solar cells stable. Nature *544*, 155–156.

28. Liu, L., Huang, S., Lu, Y., Liu, P., Zhao, Y., Shi, C., Zhang, S., Wu, J., Zhong, H., Sui, M., et al. (2018). Grain-Boundary "patches" by in situ conversion to enhance perovskite solar cells stability. Adv. Mater. *30*, 1800544.

29. Lee, J.W., Kim, S.G., Bae, S.H., Lee, D.K., Lin, O., Yang, Y., and Park, N.G. (2017). The interplay between trap density and hysteresis in planar heterojunction perovskite solar cells. Nano Lett. *17*, 4270–4276.

30. McMeekin, D.P., Wang, Z., Rehman, W., Pulvirenti, F., Patel, J.B., Noel, N.K., Johnston, M.B., Marder, S.R., Herz, L.M., and Snaith, H.J. (2017). Crystallization kinetics and morphology control of formamidinium–cesium mixed-cation lead mixed-halide perovskite via tunability of the colloidal precursor solution. Adv. Mater. *29*, 1607039.

31. Guerra, V.L.P., Altamura, D., Trifiletti, V., Colella, S., Listorti, A., Giannuzzi, R., Pellegrino,

G., Condorelli, G.G., Giannini, C., Gigli, G., et al. (2015). Implications of TiO2surface functionalization on polycrystalline mixed halide perovskite films and photovoltaic devices. J. Mater. Chem. A *3*, 20811–20818.

32. Boyd, C.C., Cheacharoen, R., Leijtens, T., and McGehee, M.D. (2018). Understanding degradation mechanisms and improving stability of perovskite photovoltaics. Chem. Rev. *119*, 3418–3451.

33. Chen, Y., Yang, Z., Wang, S., Zheng, X., Wu, Y., Yuan, N., Zhang, W.H., and Liu, S.F. (2018). Design of an inorganic mesoporous hole-transporting layer for highly efficient and stable inverted perovskite solar cells. Adv. Mater. *30*, 1805660.

34. Seo, S., Jeong, S., Bae, C., Park, N.G., and Shin, H. (2018). Perovskite solar cells with inorganic electron- and hole-transport layers exhibiting long-term (≈500 h) stability at 85 °C under continuous 1 sun illumination in ambient air. Adv. Mater. *30*, 1801010.

35. Jeon, N.J., Na, H., Jung, E.H., Yang, T.-Y., Lee, Y.G., Kim, G., Shin, H.-W., Il Seok, S., Lee, J., and Seo, J. (2018). A fluorene-terminated hole-transporting material for highly efficient and stable perovskite solar cells. Nat. Energy *3*, 682–689.

36. Mei, A., Li, X., Liu, L., Ku, Z., Liu, T., Rong, Y., Xu, M., Hu, M., Chen, J., Yang, Y., et al. (2014). A hole-conductor-free, fully printable mesoscopic perovskite solar cell with high stability. Science *345*, 295–298.

37. Wang, R., Mujahid, M., Duan, Y., Wang, Z.-K., Xue, J., and Yang, Y. (2019). A review of perovskites solar cell stability. Adv. Funct. Mater. 1808843.

38. Cao, J., Li, C., Lv, X., Feng, X., Meng, R., Wu, Y., and Tang, Y. (2018). Efficient grain boundary suture by low-cost tetra-ammonium zinc phthalocyanine for stable perovskite solar cells with expanded photoresponse. J. Am. Chem. Soc. *140*, 11577–11580.

39. Lee, J.W., Kim, H.S., and Park, N.G. (2016). Lewis acid-base adduct approach for high efficiency perovskite solar cells. Acc. Chem. Res. *49*, 311–319.

40. Wu, Y., Yang, X., Chen, W., Yue, Y., Cai, M., Xie, F., Bi, E., Islam, A., and Han, L. (2016). Perovskite solar cells with 18.21% efficiency and area over 1 cm2 fabricated by heterojunction engineering. Nat. Energy *1*, 16148.

41. Niu, T., Lu, J., Munir, R., Li, J., Barrit, D., Zhang, X., Hu, H., Yang, Z., Amassian, A., Zhao, K., et al. (2018). Stable high-performance perovskite solar cells via grain boundary passivation. Adv. Mater. *30*, 1706576.

42. Zuo, L., Guo, H., deQuilettes, D.W., Jariwala, S., De Marco, N., Dong, S., DeBlock, R., Ginger, D.S., Dunn, B., Wang, M., et al. (2017). Polymer-modified halide perovskite films for efficient and stable planar heterojunction solar cells. Sci. Adv. *3*, e1700106.

43. Lee, J.W., Dai, Z., Lee, C., Lee, H.M., Han, T.H., De Marco, N., Lin, O., Choi, C.S., Dunn, B., Koh,

J., et al. (2018). Tuning molecular interactions for highly reproducible and efficient formamidinium perovskite solar cells via adduct approach. J. Am. Chem. Soc. *140*, 6317–6324.

44. Xiang, W., Chen, Q., Wang, Y., Liu, M., Huang, F., Bu, T., Wang, T., Cheng, Y.B., Gong, X., Zhong, J., et al. (2017). Improved air stability of perovskite hybrid solar cells via blending poly(dimethylsiloxane)-urea copolymers. J. Mater. Chem. A *5*, 5486–5494.

45. Lee, J.W., Bae, S.H., Hsieh, Y.T., De Marco, N., Wang, M., Sun, P., and Yang, Y. (2017). A bifunctional Lewis base additive for microscopic homogeneity in perovskite solar cells. Chem *3*, 290–302.

46. Arora, N., Dar, M.I., Hinderhofer, A., Pellet, N., Schreiber, F., Zakeeruddin, S.M., and Grätzel, M. (2017). Perovskite solar cells with CuSCN hole extraction layers yield stabilized efficiencies greater than 20%. Science *358*, 768–771.

47. Singh, B.R., Wechter, M.A., Hu, Y., and Lafontaine, C. (1998). Determination of caffeine content in coffee using Fourier transform infra-red spectroscopy in combination with attenuated total reflectance technique: a bioanalytical chemistry experiment for biochemists. Biochem. Educ. *26*, 243–247.

48. Hou, X., Huang, S., Ou-Yang, W., Pan, L., Sun, Z., and Chen, X. (2017). Constructing efficient and stable perovskite solar cells via interconnecting perovskite grains. ACS Appl. Mater. Interfaces *9*, 35200–35208.

49. Lee, J.-W., Dai, Z., Han, T.-H., Choi, C., Chang, S.-Y., Lee, S.-J., De Marco, N., Zhao, H., Sun, P., Huang, Y., et al. (2018). 2D perovskite stabilized phase-pure formamidinium perovskite solar cells. Nat. Commun. *9*, 3021.

50. Jiang, Q., Zhang, L., Wang, H., Yang, X., Meng, J., Liu, H., Yin, Z., Wu, J., Zhang, X., and You, J. (2017). Enhanced electron extraction using SnO2 for high-efficiency planar-structure HC(NH2)2PbI3-based perovskite solar cells. Nat. Energy *2*, 16177.

51. Han, Q., Hsieh, Y.T., Meng, L., Wu, J.L., Sun, P., Yao, E.P., Chang, S.Y., Bae, S.H., Kato, T., Bermudez, V., et al. (2018). High-performance perovskite/ Cu(In,Ga)Se2monolithic tandem solar cells. Science *361*, 904–908.

52. Bi, E., Chen, H., Xie, F., Wu, Y., Chen, W., Su, Y., Islam, A., Grätzel, M., Yang, X., and Han, L. (2017). Diffusion engineering of ions and charge carriers for stable efficient perovskite solar cells. Nat. Commun. *8*, 15330.

53. Kim, T.W., Shibayama, N., Cojocaru, L., Uchida, S., Kondo, T., and Segawa, H. (2018). Real-time in situ observation of microstructural change in organometal halide perovskite induced by thermal degradation. Adv. Funct. Mater. *28*, 1804039.

Supplemental Information

Caffeine Improves the Performance

and Thermal Stability

of Perovskite Solar Cells

Rui Wang, Jingjing Xue, Lei Meng, Jin-Wook Lee, Zipeng Zhao, Pengyu Sun, Le Cai, Tianyi Huang, Zhengxu Wang, Zhao-Kui Wang, Yu Duan, Jonathan Lee Yang, Shaun Tan, Yonghai Yuan, Yu Huang, and Yang Yang
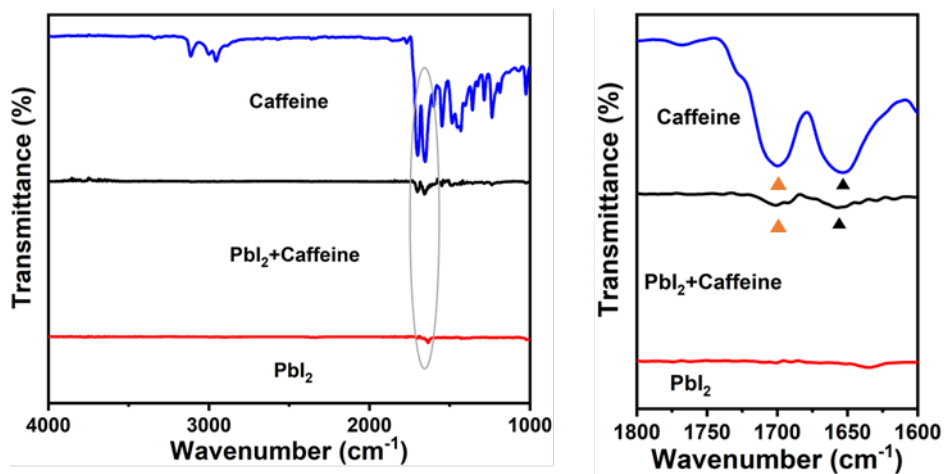
Figure S1 FTIR spectra and fingerprint regions of pure caffeine, caffeine-PbI$_2$ and the pristine

PbI$_2$ films. The triangles indicate the stretching vibration peaks of C=O in the two films.
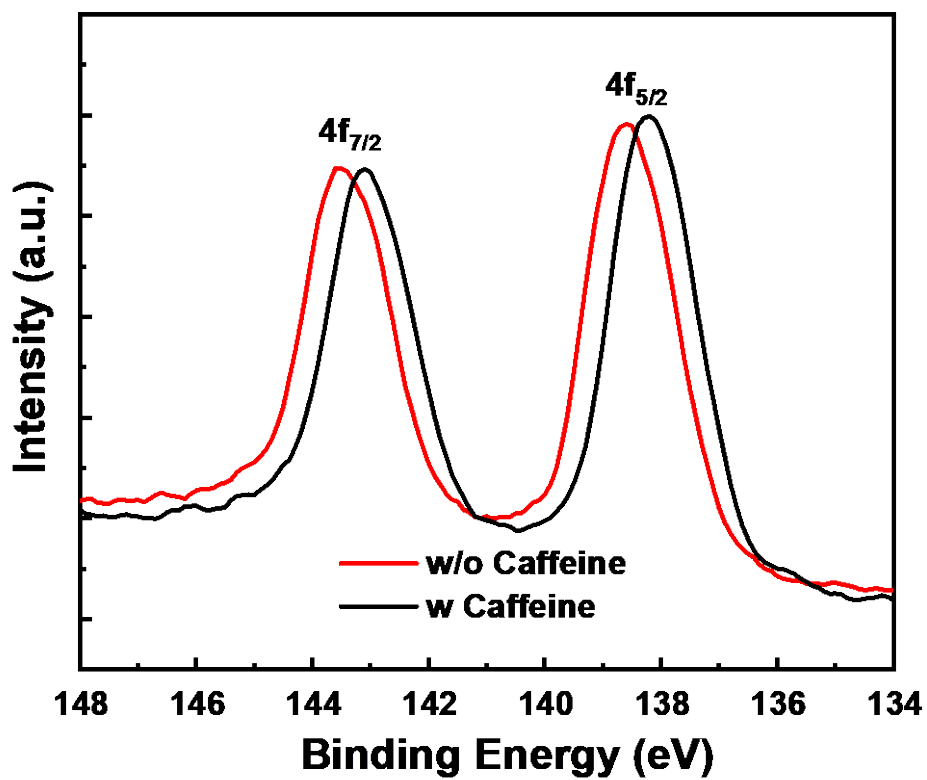
Figure S2. XPS data for Pb 4f 7/2 and Pb 4f 5/2 core level spectra in MAPbI$_3$ and MAPbI$_3$: Caffeine films.
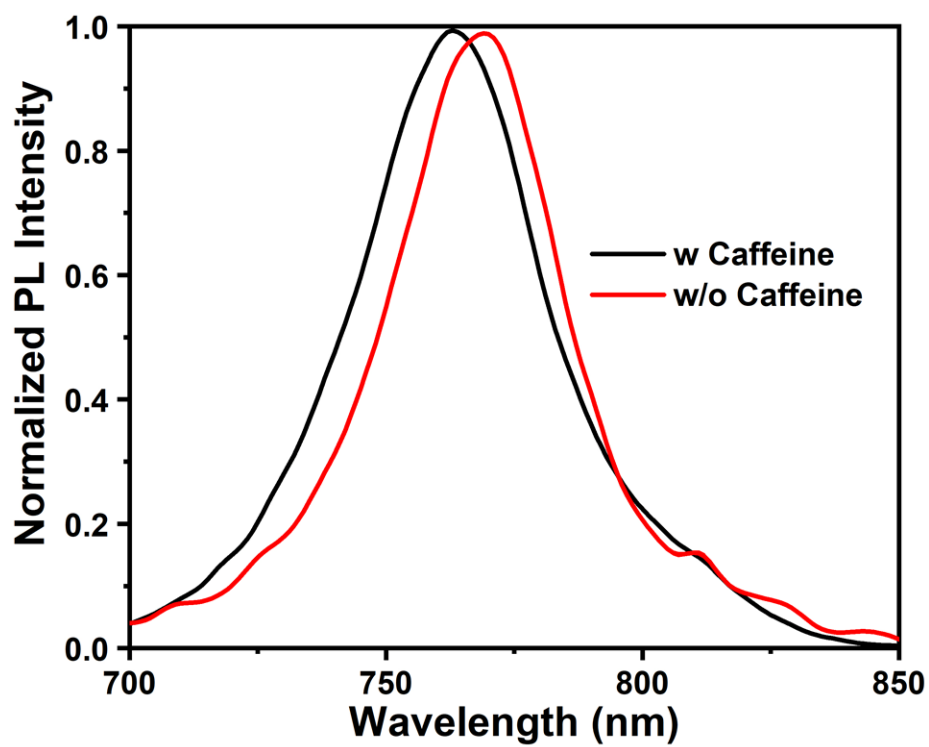
Figure S3 Normalized Steady-State PL spectra of PVSK films without and with caffeine.

a.
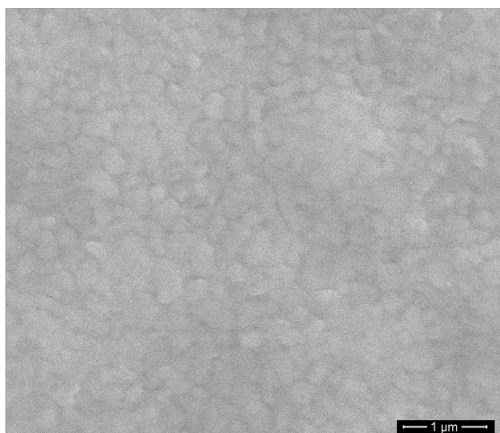
b.
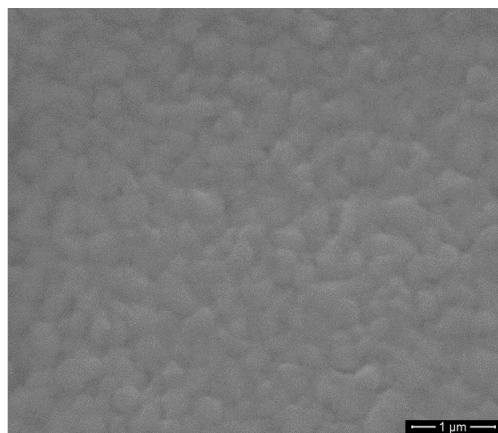
Figure S4 Top-view SEM of the a. Pure PVSK film and b. PVSK-Caffeine film

a.

b.
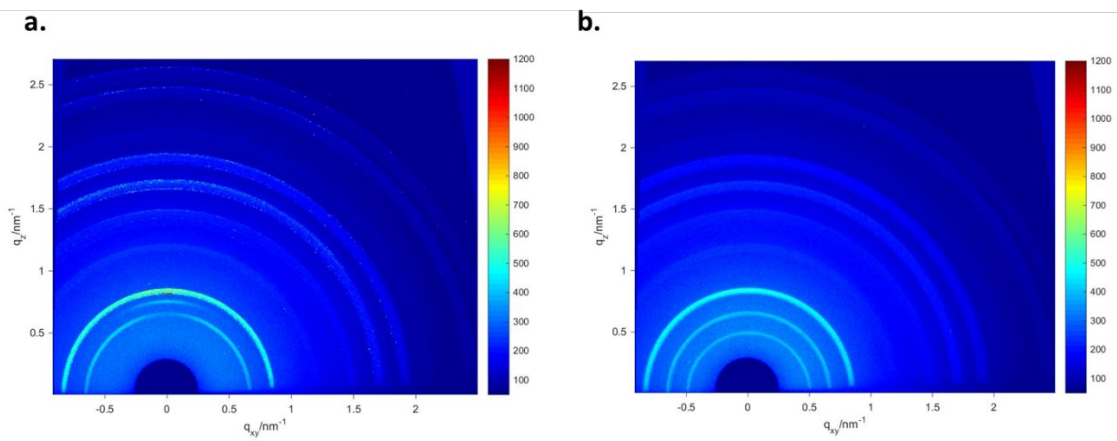
Figure S5 2D GIWAXS Patterns of the PVSK films: a. without caffeine; b. with caffeine.
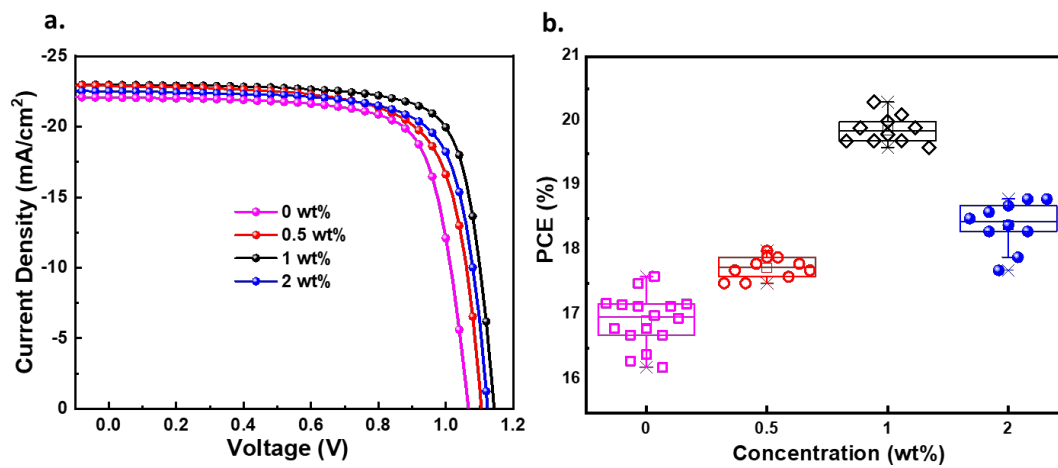
Figure S6 a. *J-V* curves of the PVSK with different concentration of caffeine in reverse scan direction. b. The statistic distribution of PCEs versus the concentaion of caffeine.
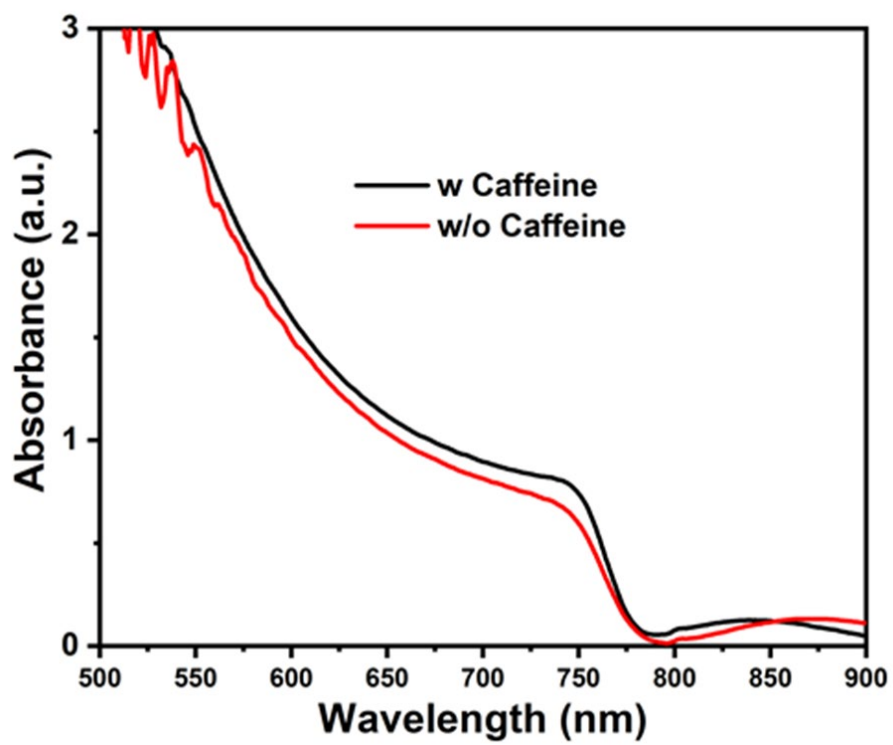
Figure S7 UV-vis spectra of PVSK films with or without caffeine.
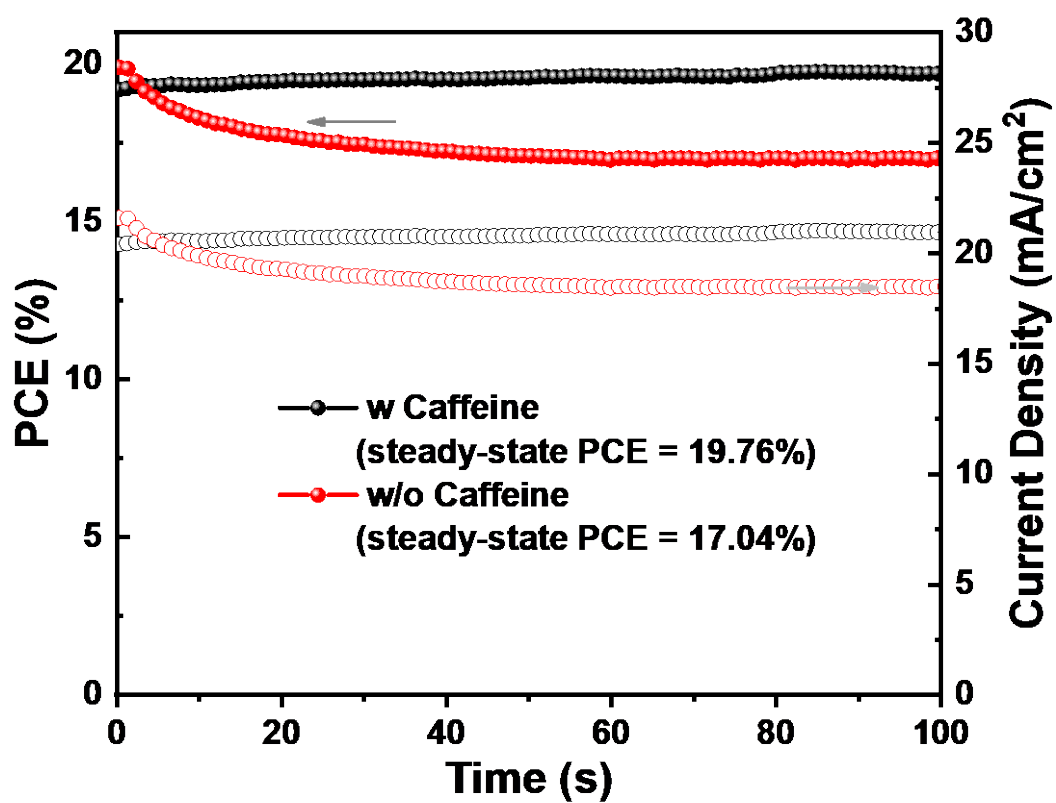
Figure S8 Steady-state PCE of the champion device based on MAPbI$_3$ and MAPbI$_3$-Caffeine
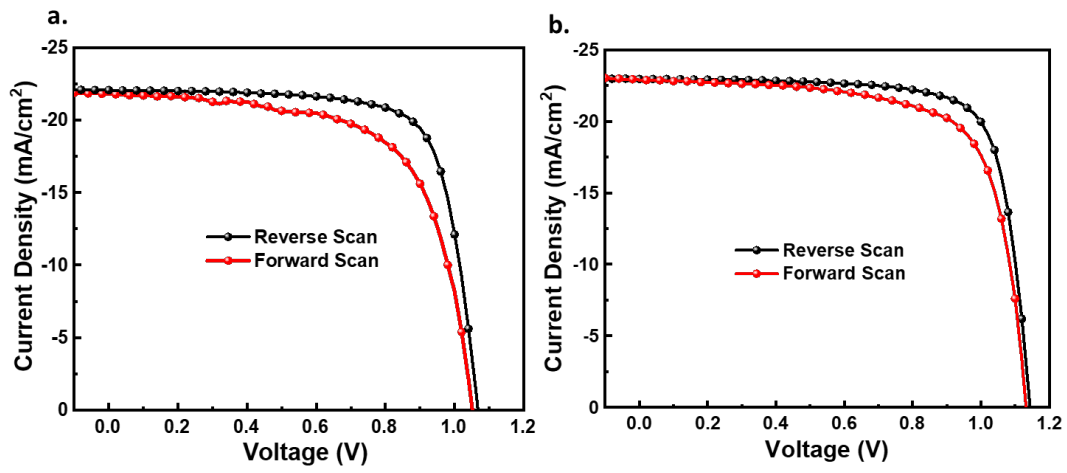
Figure S9 *J-V* curves of a. Pure MAPbI₃ device and b. Caffeine containing MAPbI₃ device on both reverse and forward scan directions.
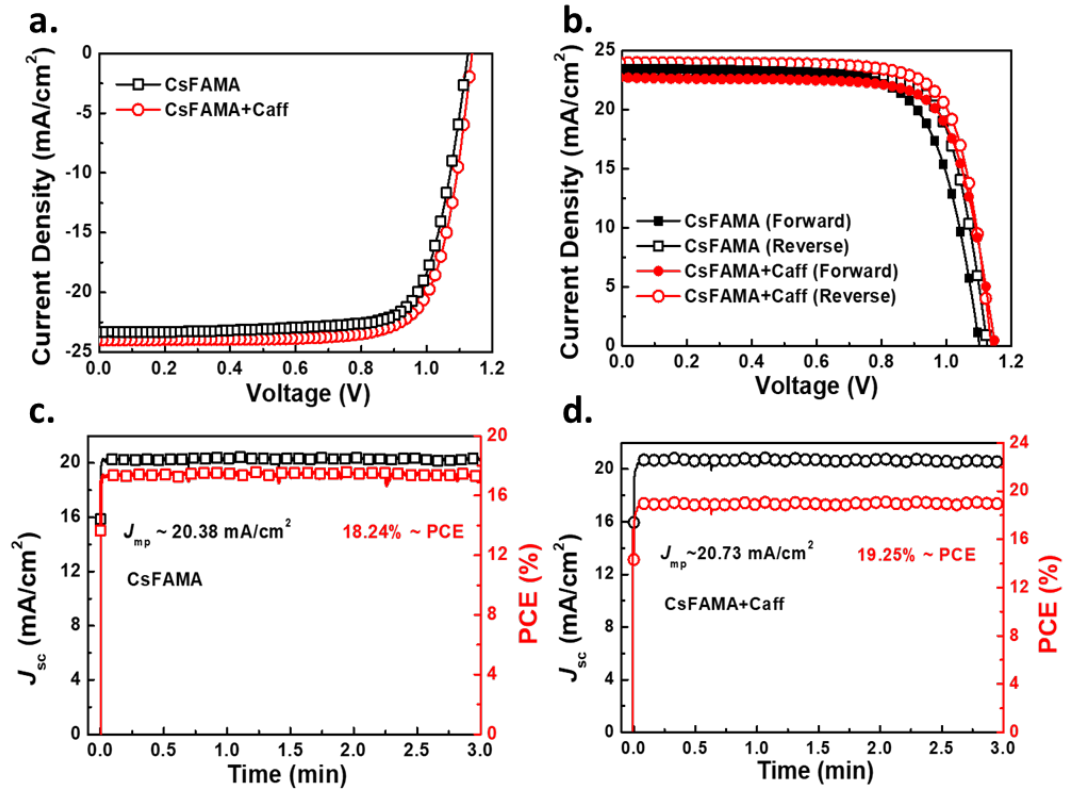
Figure S10 a. *J-V* curves under Reverse Scan of the CsFAMA based devices with or without caffeine. b. Hysteresis behaviors of the CsFAMA based devices with or without caffeine. Steady-State output efficiencies of CsFAMA based devices c. without caffeine and d. with caffeine.
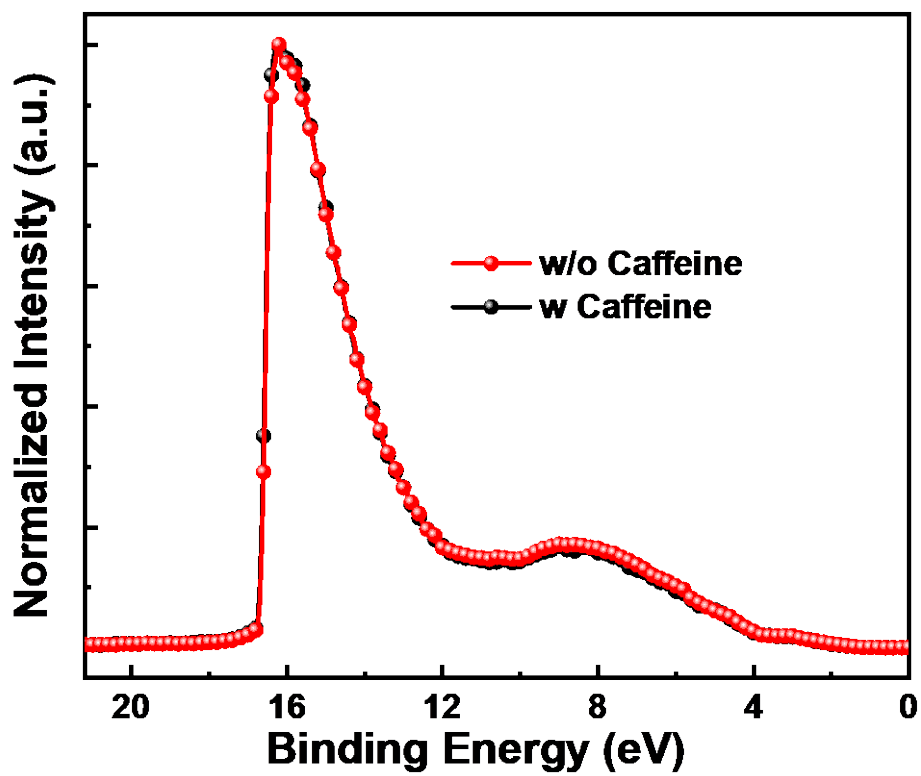
Figure S11 UPS spectra of PVSK films with or without caffeine.
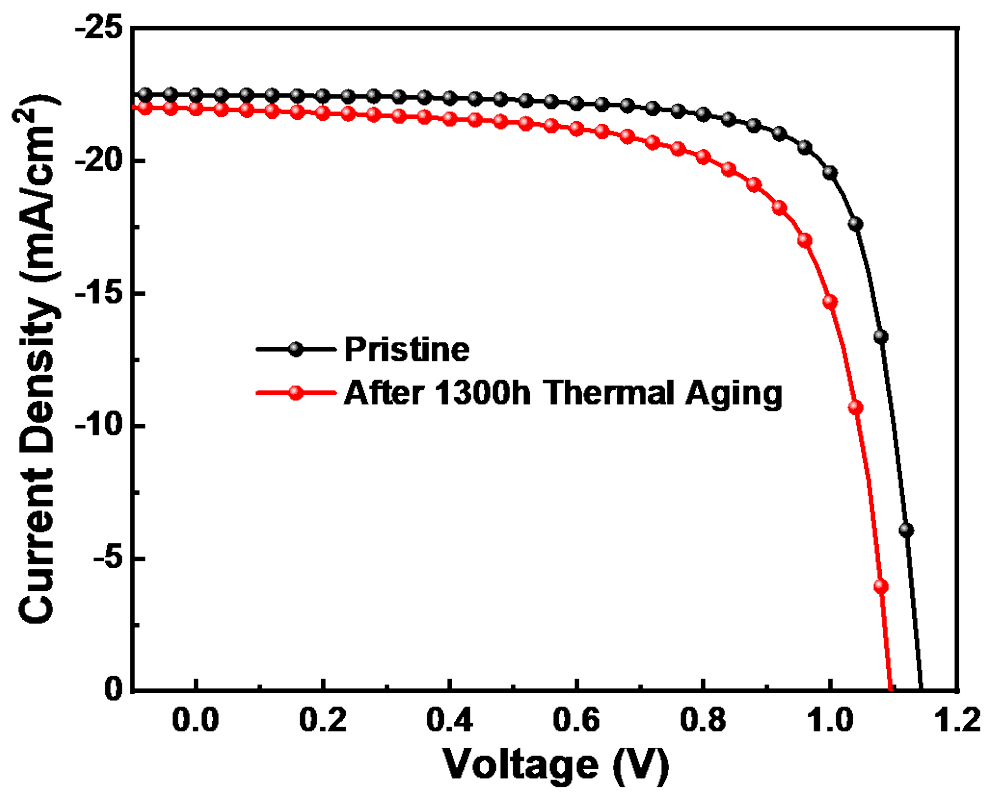
Figure S12 *J-V* curves of the selected device before and after subjected to the thermal stability test
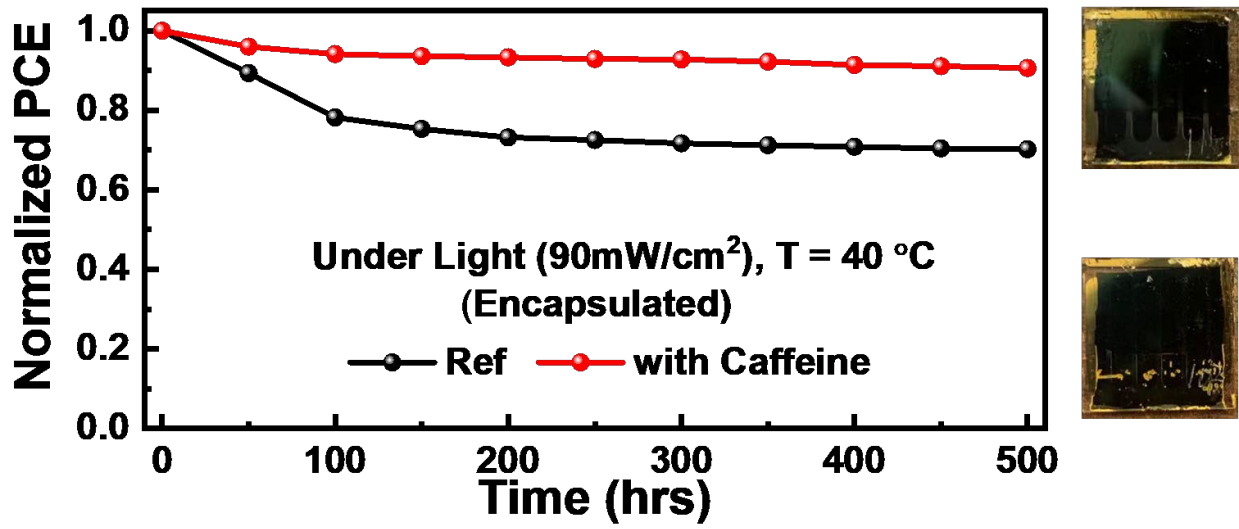
Figure S13 Evolution of the PCEs measured from the encapsulated perovskite solar cells with or without caffeine exposed to continuous light (90 ± 5 mW cm^{-2}) under open-circuit condition.
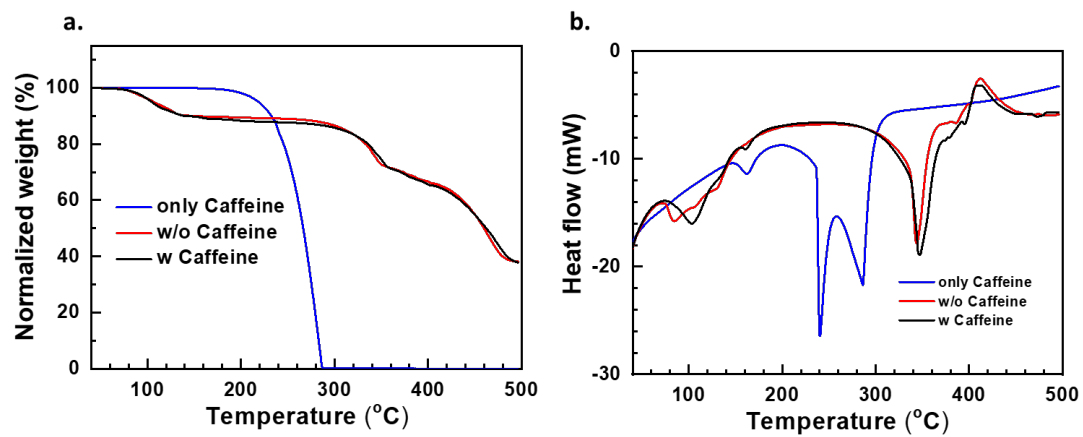
Figure S14 Full data of the TGA analysis on the pristine caffeine, MAI-PbI$_2$-DMSO adduct powder and MAI-PbI$_2$-DMSO-Caffeine adduct powder.
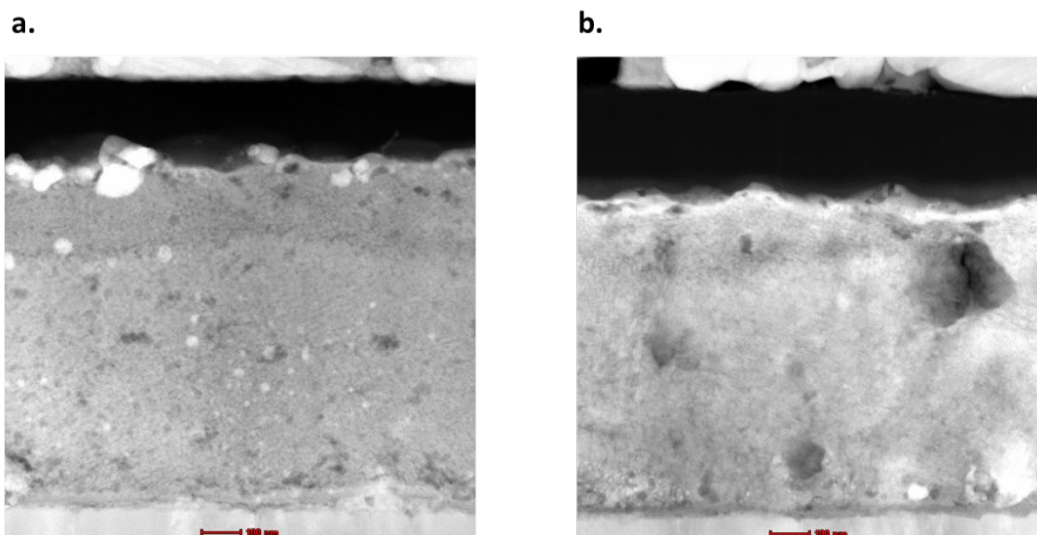
Figure S15 HAADF TEM data on the EDX mapping region of a. Pure PVSK device and b.
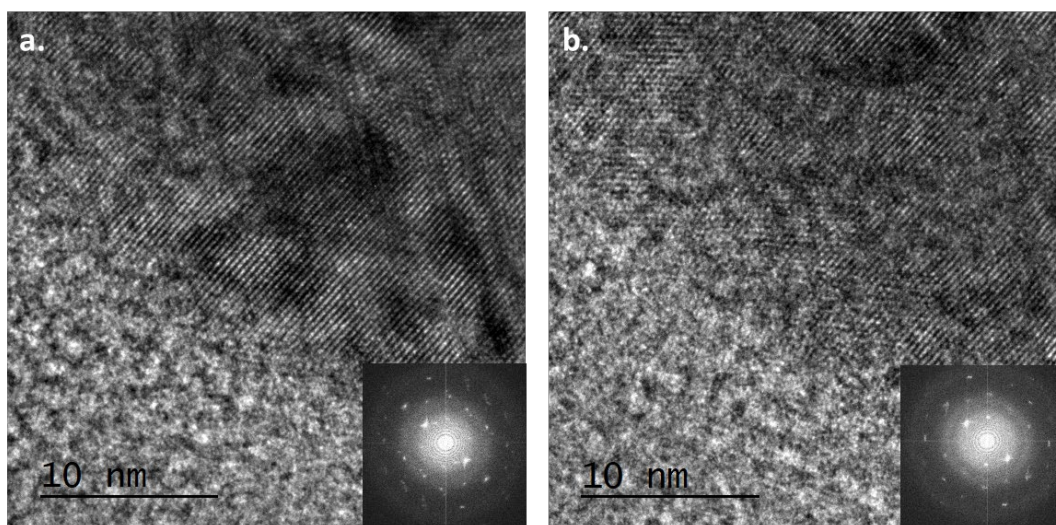
PVSK-Caffeine device.

Figure S16 HRTEM data of different Region of the PVSK-caffeine film a. before and b. after subjected to in-situ heating test.
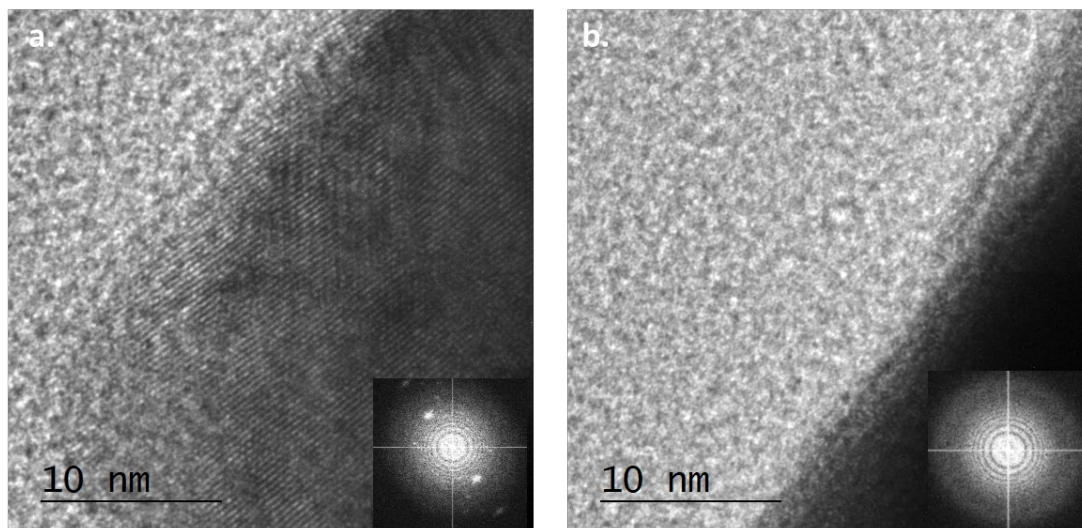
Figure S17 HRTEM data of different Region of the pure PVSK film a. before and b. after subjected to in-situ heating test.
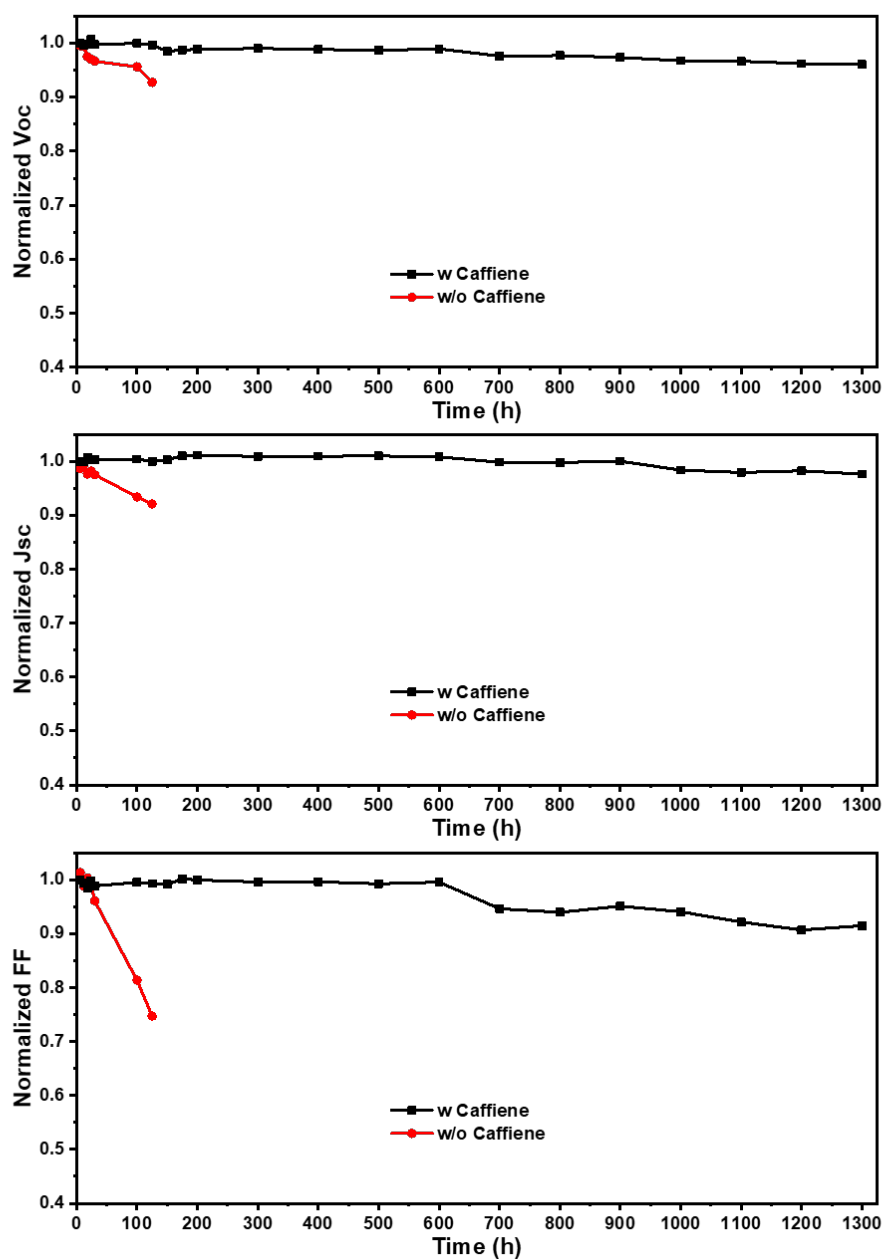
Figure S18 Evolution of the photovoltaic parameters of the device thermal stability upon 85°C continuous annealing in nitrogen box.
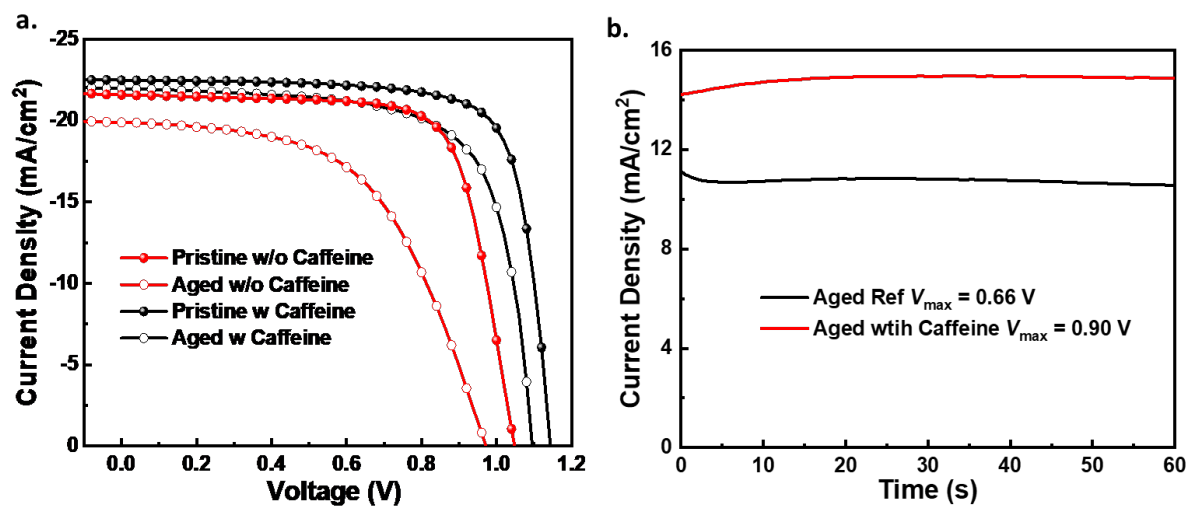
Figure S19 a. *J-V* curves under reverse scan of fresh and aged control or caffeine devices. b.

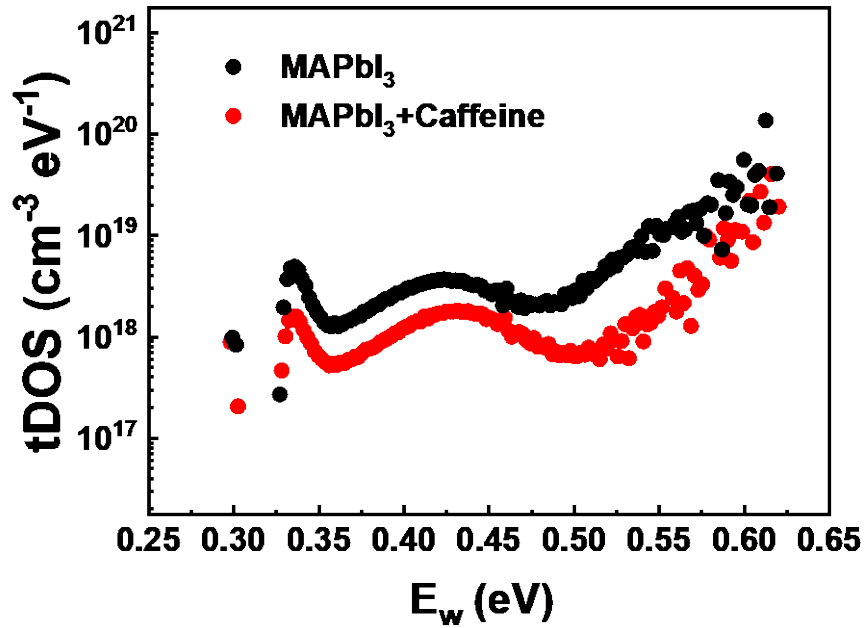Stabilized efficiency of aged control or caffeine devices.

Supplementary Note1

Figure S20 Trap density of states (*t*DOS) in perovskite-based devices with or without

caffeine

The trap density of states (*t*DOS) can be deduced from the angular frequency dependent

capacitance by the equation:

$$N_T E_\omega = -\frac{V_{bi}}{qW}\frac{dC}{d\omega}\frac{\omega}{k_B T} \quad \text{Eq S1}$$

where k_B is the Boltzmann's constant, q is the elementary charge, T is the temperature, V_{bi} and

W are obtained from the Mott-Schottky analysis, and the angular frequency ω is defined by

the following relation:

$$E_\omega = k_B T \ln\frac{\omega_0}{\omega} \quad \text{Eq S2}$$

where ω_0 is the attempt-to-escape frequency. Combining the Eq S1 and Eq. S2, the *t*DOS

level in different perovskite films can be obtained. As shown in Figure S19, the *t*DOS as a

function of the defect energy demonstrated that caffeine could reduce the deep-level defect

traps even more. The shallow-level defect traps that are deeper in perovskite films could also

be passivated by caffeine.[1,2]

Table S1. Cell parameters in the PSCs with or without scanned from forward (FS) and reverse (RS) directions.

Active layer	Scan Direction	V_{OC} (V)	J_{SC} (mA cm^{-2})	FF (%)	PCE (%)
w/o Caffeine	RS	1.067	22.08	74.29	17.50
	FS	1.051	21.80	64.85	14.85
W Caffeine	RS	1.143	22.97	77.13	20.25
	FS	1.132	22.87	70.64	18.29

Table S2 Summarized photovoltaic performance of perovskite devices with or without caffeine.

Devices		V_{oc} (V)	J_{sc} (mA/cm^2)	FF (%)	PCE (%) (reverse)	PCE (%) (forward)
CsFAMA	Average	1.11±0.02	23.06±0.36	75±1	19.45±0.47	18.05±0.33
	Best	1.13	23.30	76	19.92	18.38
CsFAMA+Caff	Average	1.14±0.01	23.54±0.43	75±1	20.45±0.37	19.26±0.26
	Best	1.14	23.97	76	20.82	19.52

References

[1]   Ran C, Xu J, Gao W, Huang C, Dou S. Defects in metal triiodide perovskite materials towards high-performance solar cells: Origin, impact, characterization, and engineering. Chem Soc Rev 2018;47:4581–610. doi:10.1039/c7cs00868f.

[2]   Huang J, Yuan Y, Shao Y, Yan Y. Understanding the physical properties of hybrid perovskites for photovoltaic applications. Nat Rev Mater 2017;2:17042. doi:10.1038/natrevmats.2017.42.